AGU PUBLICATIONS

Water Resources Research

RESEARCH ARTICLE
10.1002/2013WR014331

Time-lapse borehole radar for monitoring rainfall infiltration through podosol horizons in a sandy vadose zone

Elmar Strobach[1], B. D. Harris[1], J. C. Dupuis[1,2], and A. W. Kepic[1]

[1]Department of Exploration Geophysics, Curtin University, Perth, Western Australia, Australia, [2]Now at Département de géologie et de génie géologique, Université Laval, Laval, Quebec, Canada

Key Points:
- Time-lapse borehole radar case study for water infiltration monitoring
- Podosol accumulation horizons impede wetting front development
- Combination of ZOP and VRP BHR methods can improve accuracy

Correspondence to:
E. Strobach,
elmar.strobach@postgrad.curtin.edu.au

Citation:
Strobach, E., B. D. Harris, J. C. Dupuis, and A. W. Kepic (2014), Time-lapse borehole radar for monitoring rainfall infiltration through podosol horizons in a sandy vadose zone, *Water Resour. Res.*, *50*, 2140–2163, doi:10.1002/2013WR014331.

Received 27 JUNE 2013
Accepted 6 FEB 2014
Accepted article online 12 FEB 2014
Published online 10 MAR 2014

Abstract The shallow aquifer on the Gnangara Mound, north of Perth, Western Australia, is recharged by winter rainfall. Water infiltrates through a sandy Podosol where cemented accumulation (B-) horizons are common. They are water retentive and may impede recharge. To observe wetting fronts and the influence of soil horizons on unsaturated flow, we deployed time-lapse borehole radar techniques sensitive to soil moisture variations during an annual recharge cycle. Zero-offset crosswell profiling (ZOP) and vertical radar profiling (VRP) measurements were performed at six sites on a monthly basis before, during, and after annual rainfall in 2011. Water content profiles are derived from ZOP logs acquired in closely spaced wells. Sites with small separation between wells present potential repeatability and accuracy difficulties. Such problems could be lessened by (i) ZOP saturated zone velocity matching of time-lapse curves, and (ii) matching of ZOP and VRP results. The moisture contents for the baseline condition and subsequent observations are computed using the Topp relationship. Time-lapse moisture curves reveal characteristic vadose zone infiltration regimes. Examples are (I) full recharge potential after 200 mm rainfall, (II) delayed wetting and impeded recharge, and (III) no recharge below 7 m depth. Seasonal infiltration trends derived from long-term time-lapse neutron logging at several sites are shown to be comparable with infiltration trends recovered from time-lapse crosswell radar measurements. However, radar measurements sample a larger volume of earth while being safer to deploy than the neutron method which employs a radioactive source. For the regime (III) site, where time-lapse radar indicates no net recharge or zero flux to the water table, a simple water balance provides an evapotranspiration value of 620 mm for the study period. This value compares favorably to previous studies at similar test sites in the region. Our six field examples demonstrate application of time-lapse borehole radar for characterizing rainfall infiltration.

1. Introduction

Warming over the past century may be causing changes in regional rainfall patterns [*Kundzewicz et al.*, 2007; *Timbal et al.*, 2006]. In Perth, Western Australia, the drying climate of the last 40 years has reduced the groundwater recharge from winter rainfall [*Yesertener*, 2002]. During the same period, population grew from approximately 700,000 (1971) to 1.7 million (2011) (http://www.abs.gov.au/census). These changes have led to additional water demand and therefore increased groundwater abstraction. Much of Perth's water supply is pumped from aquifers found at, or proximal to, the Gnangara Mound north of the city (Figure 1). Over the last decades, increased stresses on the groundwater supply have caused localized water table declines of up to 4 m [*Yesertener*, 2002].

Numerical modeling can improve our understanding of potential impacts of climate change and the increased water abstraction from the Gnangara Mound groundwater resource. For estimating water balance, groundwater recharge from rainfall is modeled separately with a vertical flux model (VFM) [*Xu et al.*, 2008; *Silberstein et al.*, 2009]. On top of the VFM sits a processed-based simulator developed by CSIRO called WAVES (http://www.clw.csiro.au/products/waves/). Several biophysical processes are considered for groundwater recharge calculation such as water, atmosphere, vegetation, energy, and solute transport. The success of process-based recharge modeling, however, depends on the accuracy of input parameters.

In this study, we investigate the applicability of borehole radar (BHR) techniques to monitor infiltration and to draw conclusions on preinfiltration conditions. We also evaluate the influence of water-retentive podosol horizons on wetting front development by comparing sites where impeding layers are present or absent.

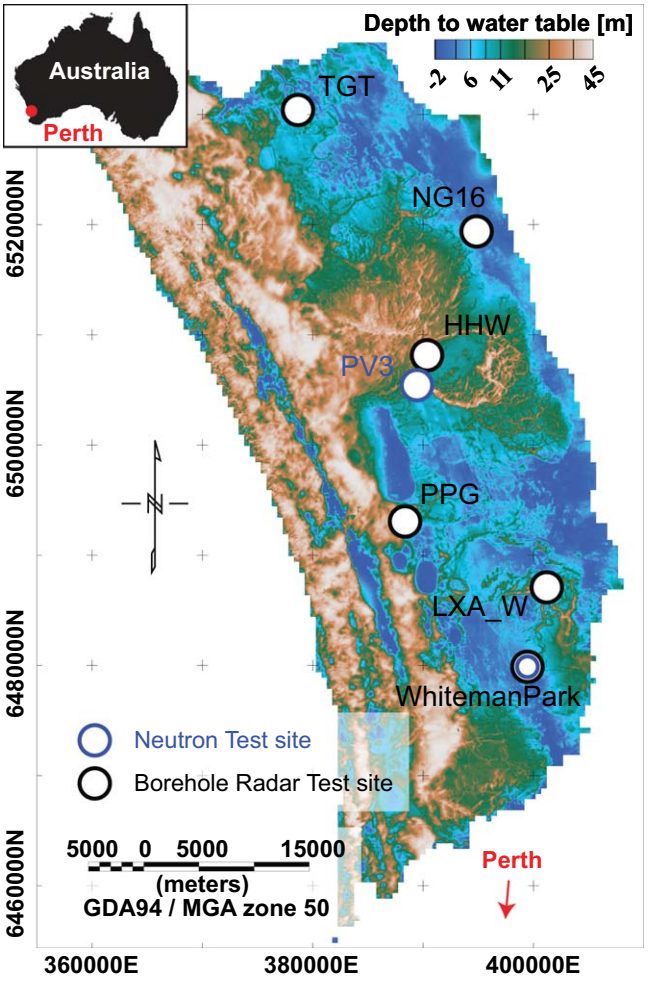

Figure 1. The Gnangara Mound north of Perth, Western Australia. The depth to water gives an indication of the topography that is dominated by sand dunes and wetlands. Black circles are test sites where time-lapse borehole radar was performed, and blue circles are sites with time-lapse neutron logging data available. Water table and topography data provided by Water Corporation (based on minimum water table 2005).

1.1. Geologic Background

The Gnangara Mound groundwater system comprises several aquifers and aquitards, including deeper aquifers of the Yaragadee and Leederville Formations. The shallow superficial water reservoirs consist of the Tamala Limestone Formation, Bassendean Sand Formation, and Guildford Clay Formation [*McArthur and Bettenay*, 1974; *Davidson*, 1995]. The main portion of recharge to the Superficial Formations comes from shallow infiltration below natural vegetation (Banksia woodland) and pasture on the Bassendean Sand [*Silberstein et al*., 2009].

In this study, we concentrate on the Bassendean Sands which are located in the central part of the Gnangara Mound. The Bassendean Formation consists of leached quartz sand with high saturated hydraulic conductivity that should facilitate high infiltration rates [*Xu et al*., 2008]. The Bassendean soil complicates infiltration, however, as it is a heterogeneous Podosol with indurated accumulation horizons showing variable degree of cementation [*Bertuch and Froend*, 2006; *Searle and Bathols*, 2009; *Strobach et al*., 2010a]. These heterogeneous layers can be water retentive [*Bertuch and Froend*, 2006] and may influence infiltration and recharge rates. They also may provide plant-available water during dry season.

A large variety of indurated sand and cemented soil horizons have been described in the literature for Australian soils [*Thompson*, 1992; *Cox et al*., 2002; *Verboom and Pate*, 2006; *Singh and Wong*, 2010]. Two different types of cemented horizons have been identified at the test sites chosen for this study: (a) an aeric Podosol B(hs) accumulation horizon of light brown to dark orange color containing humic oxyhydroxides, allophane, and/or sesquioxides (iron hydroxides) which likely formed in the unsaturated zone independent of the water table [*Thompson*, 1992; *Verboom and Pate*, 2006], and (b) an accumulation horizon around the water table characterized by dark brown color and high percentage of humic matter and allophane [*Singh and Wong*, 2010] that lead to plastic rheology when wet. The formation of the brown to orange colored, indurated sand layers in the unsaturated zone are a result of mechanical separation and illuviation of fine material [*Thompson*, 1992] and mineral leaching and precipitation (i.e., chemical accumulation) with possible influence of vegetation [*Verboom and Pate*, 2006]. Erosion processes alter the initial continuous layers [*Thompson*, 1992] and resulting pipe structures may lead to preferential flow paths [*Strobach*, 2013]. *Thompson* [1992] proposed that horizons undergo an evolution and migrate downward until they accumulate around the water table and result in the dark accumulation horizons.

A summary of petrophysical properties for aeric soil horizons is provided in *Strobach* [2013]. These indurated layers have increased water retention (e.g., higher field capacity, lower unsaturated hydraulic

conductivity) compared to clean sand, and their saturated hydraulic conductivity is comparatively lower. As such they typically contain elevated water content [*Bertuch and Froend*, 2006] that may be associated with sesquioxides [*van Dam et al*., 2002] and allophane.

For this investigation, anomalous layers at the test sites were identified from lithologic logs, borehole radar (BHR), and neutron logging (see Figure 2 and Table 1). The aim of this study was to gain insight into the influence of specific layers on field-scale infiltration.

1.2. Climate

The climate in south-western Australia is Mediterranean with long dry summers and high rainfall during winter. Average annual rainfall is approximately 800 mm, while annual pan evapotranspiration is approximately 1800 mm (see Figures 3 and 4, data source: http://www.bom.gov.au/climate/data/). *Farrington et al*. [1989, 1990] measured evapotranspiration directly with ventilated chambers for Banksia woodland and dampland, respectively, on the Gnangara Mound. They obtain average values of 666 mm per year (mm/a) (1985–1986, 77% of 865 mm rain) and 814 mm/a (1987–1988, 109% of 747 mm rain) for Banksia woodland and dampland, respectively. *Sharma et al*. [1991] apply the zero flux plane technique to calibrated time-lapse neutron logs and derive recharge rates between 5% and 20% of precipitation at eight test sites between 1985 and 1987.

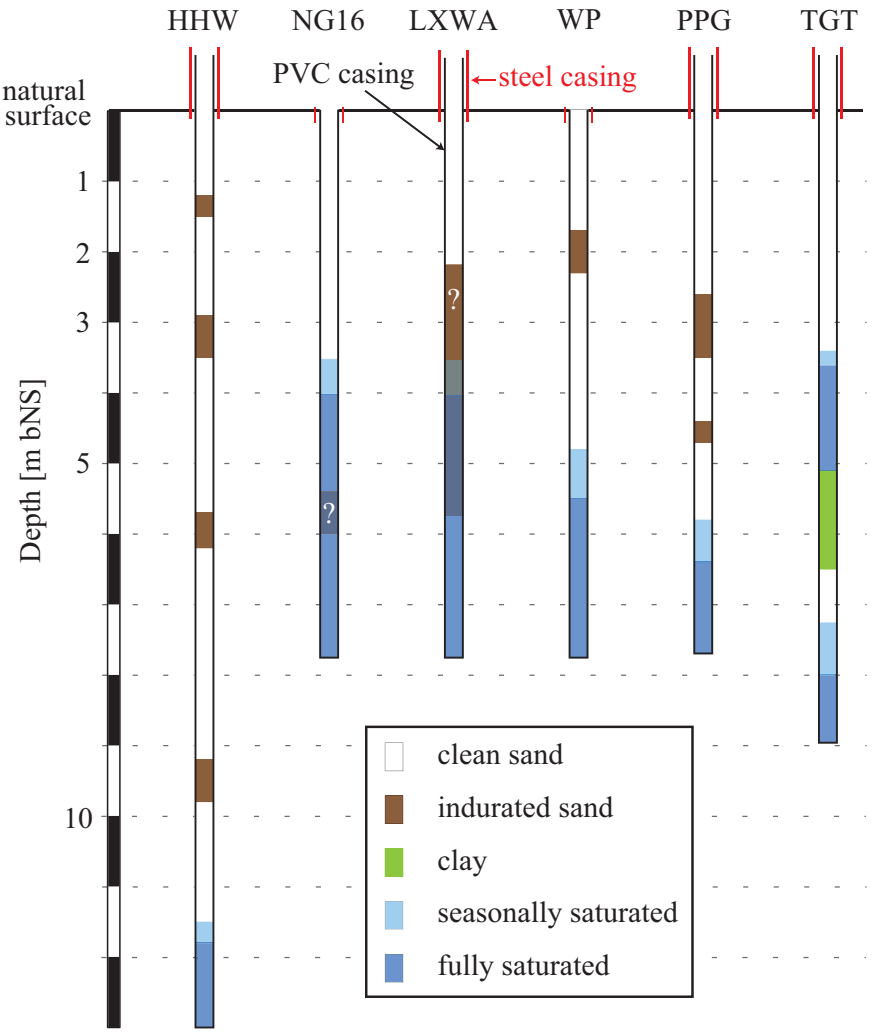

Figure 2. Soil profiles and water tables at GPR test sites as interpreted from geophysical logging, dipper measurements, and lithologic logs. Note that some boreholes have a standing outer steel casing approximately 1 m above the surface and reaching down to approximately 20 cm, while others are level with the natural surface; all have a concrete foundation.

Table 1. Test Site Characteristics Including Month of Measurements, Position of Water-Retentive Layers, Borehole Geometry, Water Table Information, and Vegetation at Site

	High Hill Road West (HHW)	North Gnangara, Airfield Road (NG16)	Lexia West (LXWA)	Whiteman Park Site 4 (WP)	Pinjar Piggery (PPG)	Tangletoe Swamp (TGT)
Date of experiments (month)	5, 6, 8, 9, 10, 12, 3	4, 7, 8, 9	5, 7, 8, 9	4, 7, 8, 9	5, 6, 8, 9, 10, 3	5, 7, 8
Borehole separation (m)	0.98	4.85	2 (4.05)	11.5	1.17	1.95 (3.54)
Depth to water table (m)	11.5	4–3.5	4–3.5	4.8–5.5	5.8–6.4	3.4–3.6
Indurated sand intervals in vadose zone (m bNS)	[1.2–1.5] [2.9–3.5] [5.7–6.2] [9.2–9.8]		o (below 2 m?)	[1.7–2.3]	[2.6–3.5] [4.4–4.7]	
Vegetation	+	−	+	+	−/o	O
Comments	Naturally vegetated	Not vegetated, close to elevated street, possible runoff onto test site	Naturally vegetated but thinned at site, trees at close distance	Naturally vegetated, winter pumping trial	Poorly vegetated, some reestablished vegetation after logging of pine trees	Gap in vegetation, natural vegetation close

1.3. Borehole Radar

Borehole radar (BHR) is a geophysical technique based on electromagnetic wave propagation and reflection that is akin to ground penetrating radar (GPR) [*Huisman et al*., 2003]. It has found wide application in the field of hydrogeophysics as it enables water content quantification [e.g., *Lambot et al*., 2008, and references therein]. Electromagnetic wave propagation at radar frequencies (1 MHz to a few GHz) is controlled by the dielectric properties of the sampled medium [*Olhoeft*, 1981]. Dry sands, composed of a mixture of minerals such as quartz or feldspar and air, have low relative dielectric permittivity values ϵ_r that range between 2 and 6 [*Davis and Annan*, 1989]. Water, in contrast, has a very large relative dielectric permittivity of $\epsilon_r = 80$ at 20°C (in liquid form increasing with decreasing temperature) [*Davis and Annan*, 1989]. Thus, soil moisture content has a large impact on the bulk dielectric permittivity of mixed granular media. Various models have been proposed to derive volumetric water content from dielectric permittivity [*Topp et al*., 1980; *Huisman et al*., 2003; *Brovelli and Cassiani*, 2008; *Steelman and Endres*, 2011]. We chose the empirical Topp relationship [*Topp et al*., 1980] for conversion from dielectric permittivity to water content as it provides reasonable fit to laboratory measurements for this environment [*Strobach*, 2013].

The GPR technique is most suited for environments with low electrical conductivity. Salt water, wet clay minerals, and other electrically conductive materials greatly attenuate electromagnetic waves in the radar frequency band [*Davis and Annan*, 1989]. A crucial part of planning a successful GPR survey is to estimate the range of possible subsurface electrical conductivities at a site and to infer the depth of penetration [*Davis and Annan*, 1989]. For clays or salt water, depth of penetration can tend to zero. In dry quartz sand or sand saturated with fresh water, on the other hand, the depth of penetration can be several meters to tens of meters [*Davis and Annan*, 1989]. Such an electrically resistive medium typically has a low dielectric loss as well. In this case, the real dielectric permittivity determines propagation velocity of the emitted radar pulse. Analysis of experimental field data is therefore often based on travel times of direct, reflected or refracted wave arrivals to derive a subsurface velocity model to derive a permittivity distribution.

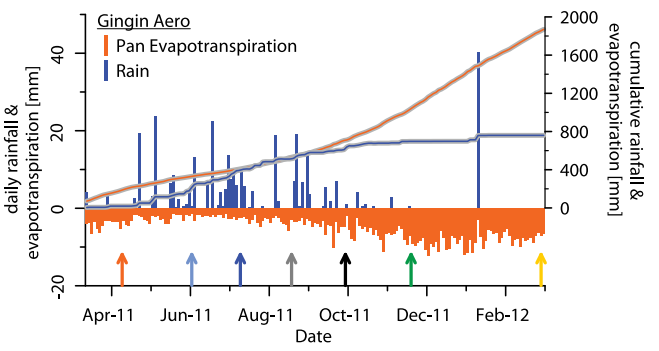

Figure 3. Daily and cumulative rainfall and evapotranspiration 2011 shown as bar chart and line plots, respectively, in blue and orange. The annual rainfall distribution in Western Australia is Mediterranean with high rainfall events in winter (June–September) and long dry summer. Colored arrows indicate dates when borehole radar time-lapse experiments were performed (dates from High Hill Road test site). Measurements were performed before, during and after winter rainfall to monitor onset of infiltration into the soil. Rainfall and evapotranspiration data is from the Gingin Aero climate observatory which is publicly available from http://www.bom.gov.au/climate/data/.

Time-lapse BHR (i.e., repeated BHR surveys) has been used successfully in hydrogeophysical studies, especially in unsaturated zone investigations to monitor flow [*Hubbard et al*., 1997; *Deiana et al*., 2007; *Day-Lewis et al*., 2003; *Chang et al*., 2004]. *Alumbaugh et al*. [2002] investigated the accuracy and repeatability of soil moisture inferred from crosswell radar experiments, while studies

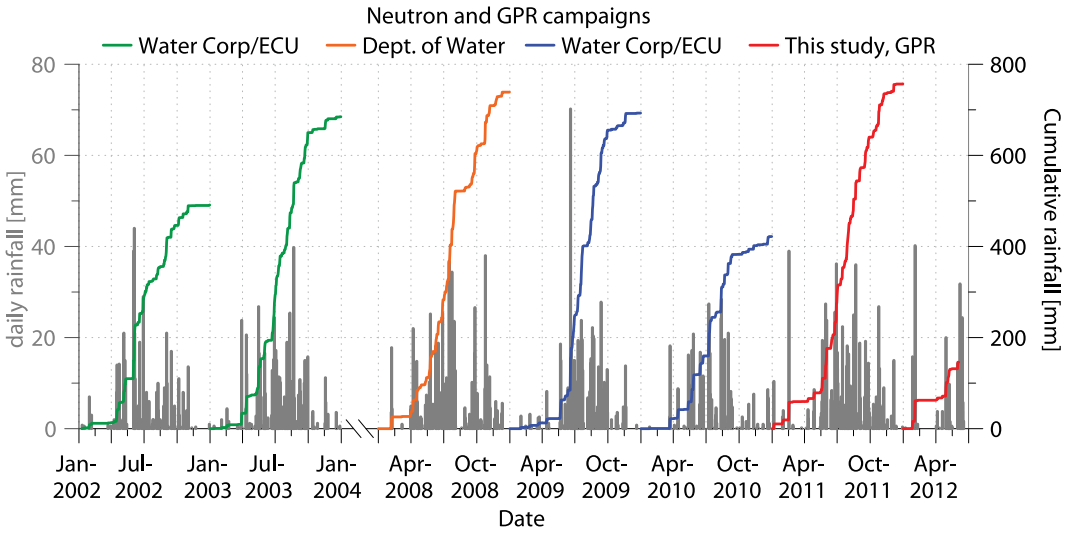

Figure 4. Daily and cumulative rainfall for years with neutron data (green, orange, and blue curves) and this study (red lines). Note the large variability throughout the years.

performed by *Binley et al.* [2001] and *Farmani et al.* [2008] monitored natural infiltration on a seasonal basis with crosswell radar.

In this study, we used zero (vertical) offset profiling (ZOP) (i.e., crosswell) [e.g., *Rucker and Ferre*, 2003] and vertical radar profiling (VRP) (i.e., single-well) [e.g., *Buursink et al.*, 2002; *Cassiani et al.*, 2008] acquisition geometry. The ZOP is a vertical scan where both antennae are lowered into the adjacent wells simultaneously while their midpoints are at the same horizontal level (see examples in Figures 5 and 7b). Vertical scans are the fastest way of obtaining a 1-D tomographic velocity profile from direct ray transmission while providing some amplitude information for attenuation analysis.

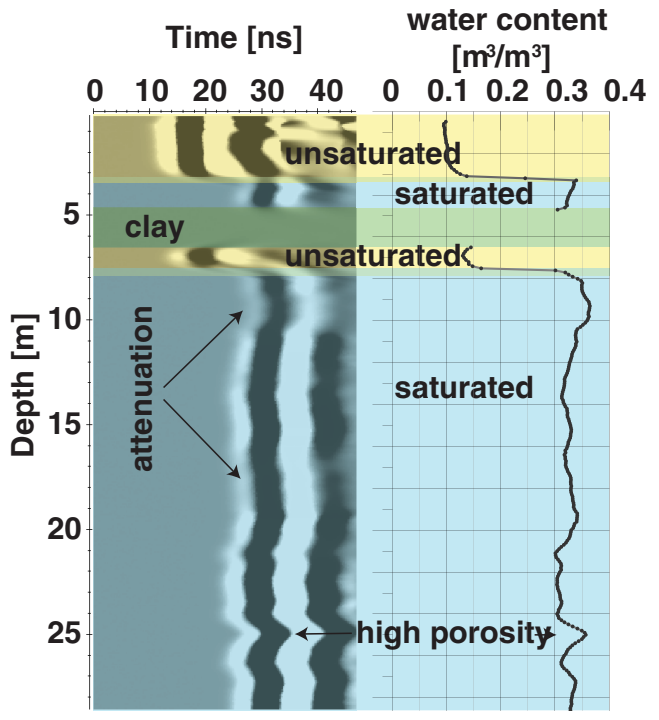

Figure 5. (left) Zero-offset crosswell profile acquired at the Tangletoe test site and (right) corresponding water content profile. The velocity profile reveals a hanging water table above a clay layer followed by a secondary unsaturated zone below the clay and a secondary water table. Note the absence of energy within the clay band and the amplitude damping below the secondary water table due to elevated clay content.

If only one borehole is available, BHR can be performed with a vertical radar profiling (VRP) geometry. In this arrangement, one antenna remains at a fixed position on the surface while the second antenna, typically the receiver, is lowered into the well (see data example in Figure 7d). The surface antenna is placed such that the radiation and sensitivity pattern of transmitting (Tx) and receiving antenna (Rx) are well coupled [*Tronicke and Knoll*, 2005]. A true zero-offset (i.e., antenna midpoint at well) is not desirable as the antennae are null-coupled in this geometry. Instead, the antenna midpoint is placed approximately 1 m from the hole.

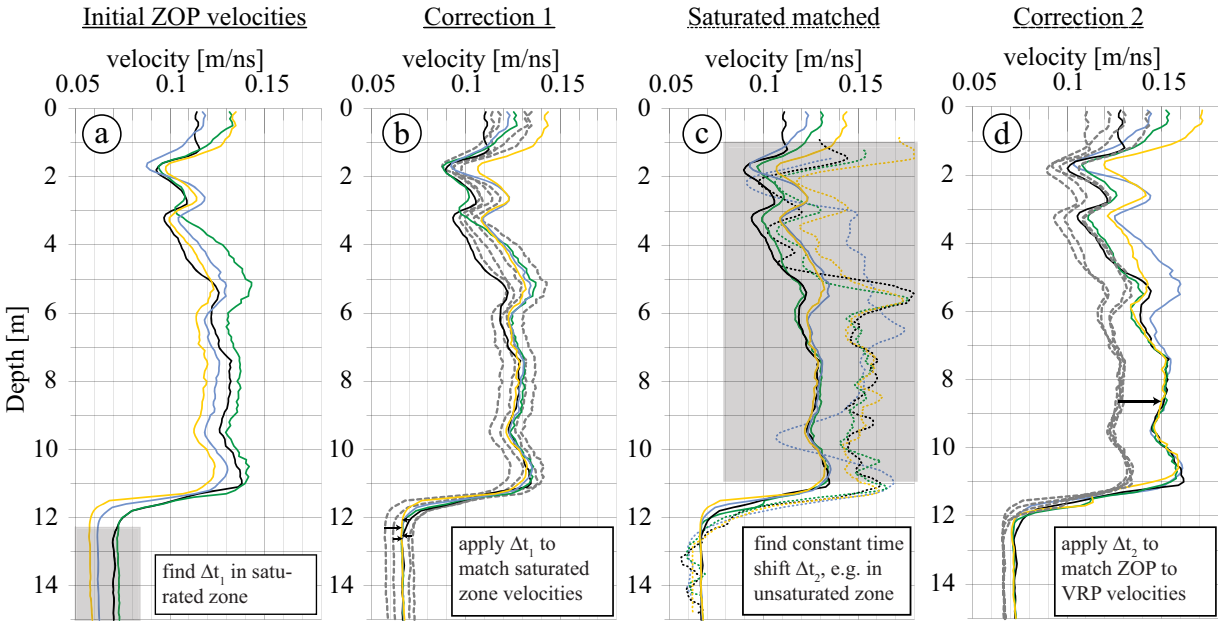

Figure 6. Schematic of matching procedure performed to correct problems with accuracy of zero-time corrections (i.e., trueness) that occurs for closely spaced wells (i.e., 1 m at HHW and PPG) if measurements are made at low frequencies (i.e., 100 MHz). First, (a) a Δt_1 is determined for every curve by least-square minimization of difference between individual curve and average travel time from saturated zone data. Then, the time shifts are applied in Figure 6b, curves now match in the saturated zone. Second, (c) the ZOP results are compared to VRP data and (d) a further constant travel time correction is applied to all ZOP curves. Note that a constant time shift has a larger influence on unsaturated zone velocities (short travel time) than on saturated zone velocities.

2. Test Sites and Field experiments

2.1. Test Sites

The BHR data were acquired at six test sites that represent a range of geologic environments present at the Bassendean Sand Formation (see site locations in Figure 1). Some sites have a podosol soil profile with well-developed water-retentive Bhs horizons that may impede water infiltration, whereas those are absent from the other sites (Figure 2). Despite the presence of potentially impeding layers, all sites are designated as medium to high groundwater recharge areas in the large-scale Perth Regional Aquifer Modelling System (PRAMS) recharge model. The most important hydrogeologic parameters for groundwater recharge estimation are the soil properties (e.g., unsaturated hydraulic conductivity, clean, or indurated sand), depth to water table, vegetation, and rainfall.

Sites Lexia West (LXWA), Tangletoe (TGT), and North Gnangara No. 16 (NG16) have shallow water tables (3–4 m below natural surface (mbNS)); Pinjar Piggery (PPG) and Whiteman Park Site 4 (WP) have intermediate depth to water table (4–7 mbNS) and High Hill Road West (HHW) a comparatively deep water table (11–12 mbNS) (Table 1, Figures 2 and 9). Sites PPG, HHW, and WP show inhomogeneous soil profiles with one to several indurated sand layers above the water table [*Searle and Bathols*, 2009; *Bertuch and Froend*, 2006]. NG16 has a clayey layer below the water table [*Pigois*, 2010; *Strobach et al.*, 2012a] and NG16 and WP have an additional radar reflector proximal to the water table that is unidentified from drill cuts. TGT has a more complex hydrogeology with a locally perched water table above a clay layer [*McHugh and Hammond*, 2011], an unsaturated horizon below the clay, followed by a second water table (regional superficial water table, Figure 5).

For BHR crosswell acquisition, the borehole separation is of great importance because it influences the resolution (Fresnel zone), occurrence of refracted energy, signal-to-noise ratio (S/N) and picking errors (details in section 3 and in the Appendix). Site WP has the largest borehole separation (11.5 m) followed by NG16 (4.8 m). TGT has a nest of four aligned holes of which we used different combinations with separations of 1.95 and 3.54 m. LXAW also has three holes in triangular arrangement with separations of 2, 4.05, and 5.74 m. Closely spaced wells are PPG (1.15 m) and HHW (0.98 m).

These wells were drilled for shallow soil investigation and not planned for geophysical crosswell experiments. Their geometry posed extra challenges in processing of the data. We show, however that excellent results may still be obtained even where geometry is suboptimal.

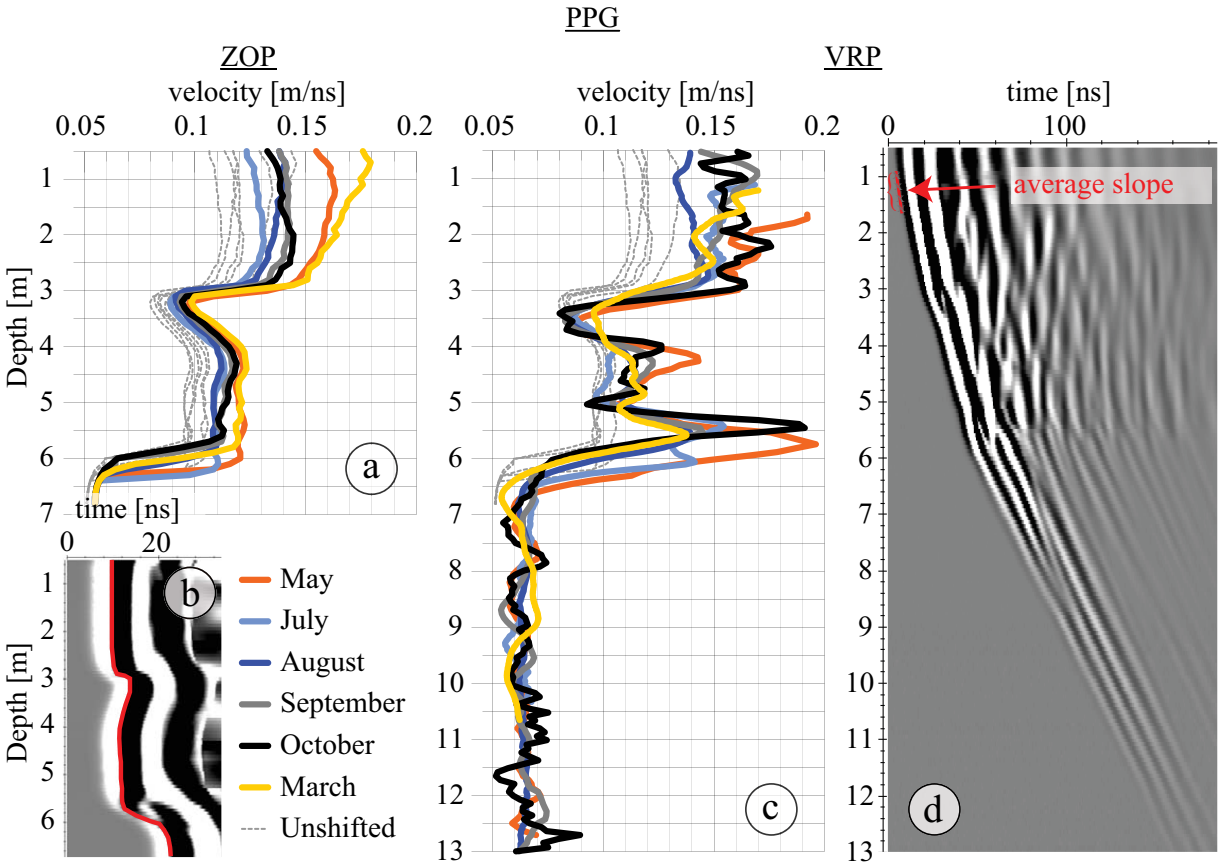

Figure 7. (a) Time-lapse ZOP results picked from the full radar waveform in (b) after saturated zone matching (dashed gray in Figure 7a and 7c) and VRP matching (colored in (a)). (c) Time-lapse VRP velocity profiles obtained from slope-analysis of the (d) VRP data.

2.2. Data Acquisition and Initial Processing

We collected BHR data before, during, and after the main recharge period that spans from autumn to spring 2011 in the southern hemisphere (see timeline in Figure 3). BHR data were acquired with the Malå ProEx 2 system, a bistatic 100 MHz slimhole antennae and a calibrated triggering wheel. A small measurement interval (1.5 cm) was chosen instead of stacking because intermittent spikes observed in the data could be more effectively removed by 2-D median filtering (sequence of 3×2, 4×1, and 1×5 samples) and subsequent stacking (from 0.015 to 0.1 m depth increment). Depth assignment is based on the antenna midpoint which is the center feedpoint of the 1.5 m long dipole antenna (0.75 m below top of dipole).

In order to preserve the amplitude and phase characteristics of the first arrivals, data processing has been kept simple. After assigning geometry to the collected radargrams, we applied simple 1-D and 2-D median filters to remove spikes [*Strobach et al.*, 2012a] before DC shift removal, zero-time correction, resampling to 0.1 ns and stacking. First arrival determination (i.e., first-break picking) for ZOPs was based on zero-crossings as they proved very repeatable as shown from repeated logging runs at 1 day (see Figure 16). For zero-time determination, the antennae were placed upright in air at constant distance x_{air} for several seconds. An average correction time t_{corr} is calculated using $t_{corr} = t_{obs} - x_{air}/c$ with t_{obs} the picked arrival time (i.e., in our case first zero-crossing, or alternatively the first arrival) and c the speed of light in vacuum ($c = 0.3$ m/ns).

After picking ZOP travel times $t_{z,i}$ (z), the ZOP interval velocities $v_{z,i}$ (z), as a function of depth z between Tx and Rx in boreholes separated by x_b (z), are calculated by:

$$v_{z,i} = \frac{x_b}{t_{z,i}}. \quad (1)$$

VRP interval velocity calculations were performed with RadexPro and are based on slope analysis within a moving window. Linear curves were fitted to the travel times over depth intervals (e.g., picks and slope indicated in Figure 7d). Note that for offset VRP, the separation x_v between Tx on the surface and Rx in the hole is related to depth by $x_v(z)=\sqrt{(x_s)^2+z^2}$ where x_s the shortest distance between surface antenna and the hole. A smoothed interval velocity curve is obtained by determining the average slope from travel times versus separation within a depth window consisting of n discrete travel times centered around depth level z_i by calculating

$$v_v(z_i)=\frac{1}{n+1}\sum_{j=i-\frac{n}{2}}^{i+\frac{n}{2}-1} v_v(z_j)=\frac{1}{n+1}\sum_{j=i-\frac{n}{2}}^{i+\frac{n}{2}-1}\frac{x_v(z_{j+1})-x_v(z_j)}{t_v(z_{j+1})-t_v(z_j)}. \quad (2)$$

The smoothing of the curve depends on the window size. We used a value of around 0.6 m, which represents a trade-off between smoothing and vertical resolution. The first average velocities are usually derived for depths greater 1.5 m because the first measurement is at depth 0.8 m, the antenna midpoint position when cable head is at surface level. Note that we used true first arrival picking for VRPs since zero-crossing picks produced unrealistic results until the antenna reached 3 m depth. We believe that this is due to interfering wavefields in the near field of the antennae. This is particularly evident for an air-refracted wave that diffracted at one of the steel casings and interfered differently with the first ground wavelet at shallow depths than at greater depths. In combination with near-field effects, this may have an impact on waveform, and therefore zero-crossings, as a function of depth.

The final processing step was to derive water content. Based on low-loss assumption, the bulk relative dielectric permittivity ϵ_r can be derived from velocity v by $\epsilon_r=c^2/v^2$, and the empirical Topp relationship [*Topp et al*., 1980]. Thus, the volumetric water content θ from dielectric permittivity was computed using the numerical inverse function for $\epsilon_r=303+93\theta+146\theta^2-76.7\theta^3$.

3. Geophysical Results

3.1. Vertical Radar Profiling

For the VRP geometry, depth of investigation depended on the test site properties, in particular depth to water table. At all sites, however, sufficient S/N was observed for reliable slope analysis of data for at least 2 m below the water table. TGT is an exception due to the clay which attenuated the EM energy and no signal penetrated beyond 5 m [*Strobach*, 2013].

At WP, we found that VRPs provide a higher vertical resolution compared to the ZOPs (ZOP well separation 11.5 m), but are less repeatable. Data and results are discussed in *Strobach et al*. [2012a]. At NG16, VRP velocity interpretation was difficult altogether [*Strobach*, 2013]. They are omitted from the discussion below. We concentrate on sites HHW and PPG and analyze VRP results from those sites.

VRP slope analysis can be unreliable at shallow depths due to uncertainty in geometry and larger influence of picking inaccuracies (see example in Figures 7c and 8b). Interfaces that create reflections (upgoing wavefields) create interference with the first arriving downgoing wavelet and extreme slopes can result. The water table is a prominent example of such a strong dielectric contrast (see, e.g., Figure 7c around 5.5 m depth, and Figure 8b around 11 m). While fk-filtering can attenuate upgoing wavefields, our experience suggests minor improvements. Therefore, anomalous velocities at interfaces have been discarded from interpretation.

Precision or repeatability (see Appendix for definition of terms) of VRPs is estimated from intervals where no change of properties is expected in time-lapse experiments. We expect that this is the case at the HHW test site between 7 and 11 m depth, and for the saturated zone at all sites.

Despite the poor repeatability observed in Figures 7c and 8b, we argue that the absolute velocities (i.e., their trueness, see Appendix B for definition of term) derived from deeper well sections are correct within their precision error. The average velocity (i.e., recovered independent of further adjustments) does not change throughout the seasons and saturated zone velocity values are randomly distributed around the average velocity (for PPG with an average error of 5.6%, see Appendix B). Their statistical distribution was tested by investigation of the difference between average velocity curve and monthly curves, which resulted in a normal distribution, a characteristic associated to random error.

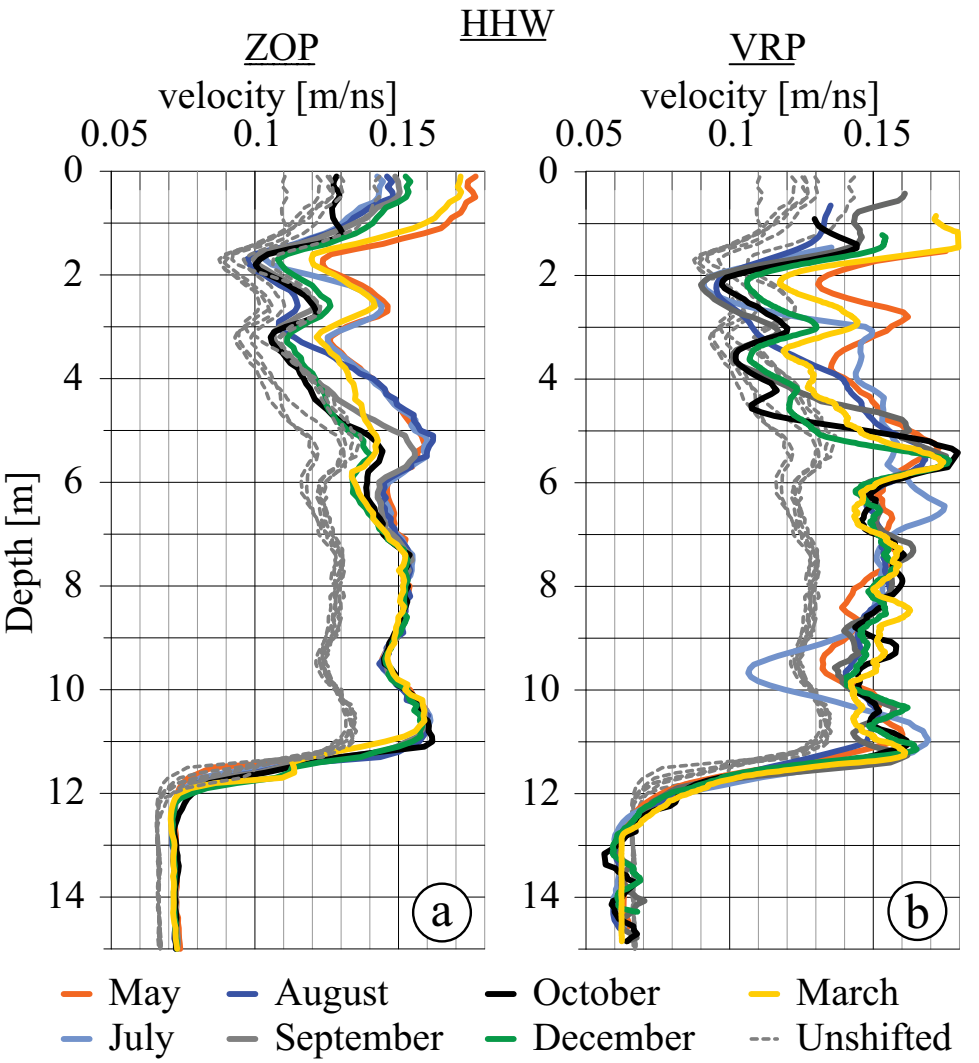

Figure 8. Time-lapse velocity profiles from the High Hill Road test site. ZOP profiles in Figure 8a show high repeatability below 7 mbNS after saturated zone matching, while the VRP curves (b) are noisier. VRP velocities above 2 m depth were not reliable, however, below 2 mbNS both techniques show the same general trend. The dashed gray curves represent initial velocity estimates for the ZOPs which are inconsistent with the VRP velocities and were therefore corrected (colored curves in Figure 8a).

Although VRP slope analysis is somewhat crude, it is largely independent of absolute travel times and by consequence, to zero-time corrections. Thus, a systematic error in velocity calculation is not expected, and therefore repeatability of absolute velocity can be achieved. This information can be used as validation or correction of other methods such as ZOP measurements.

In comparison to ZOP velocity profiles, we noticed a slight shift of VRP data, especially at HHW (Figure 8) where layers appear approximately 0.3 m lower in the VRP velocity profiles. The depth assignment has been done identical to ZOP data, that is, we used the midpoint of the dipole antenna (center feedpoint) as depth reference. The shift is evident in all time-lapse curves, which is indicative of a systematic mismatch. Currently, we do not have a proven explanation for this shift, but it may be due to energy traveling from antenna tip to tip (i.e., the upper part of the antenna dipole receives energy and slope analysis is effectively representative for the upper antenna part which would shift velocity curves upward).

3.2. Zero-Offset Profiling

Crosswell ZOP measurements revealed strong first arrivals at most sites over the full profile lengths. The only exception is the clay band at TGT between 5 and 6.5 mbNS which attenuated the signals below S/N

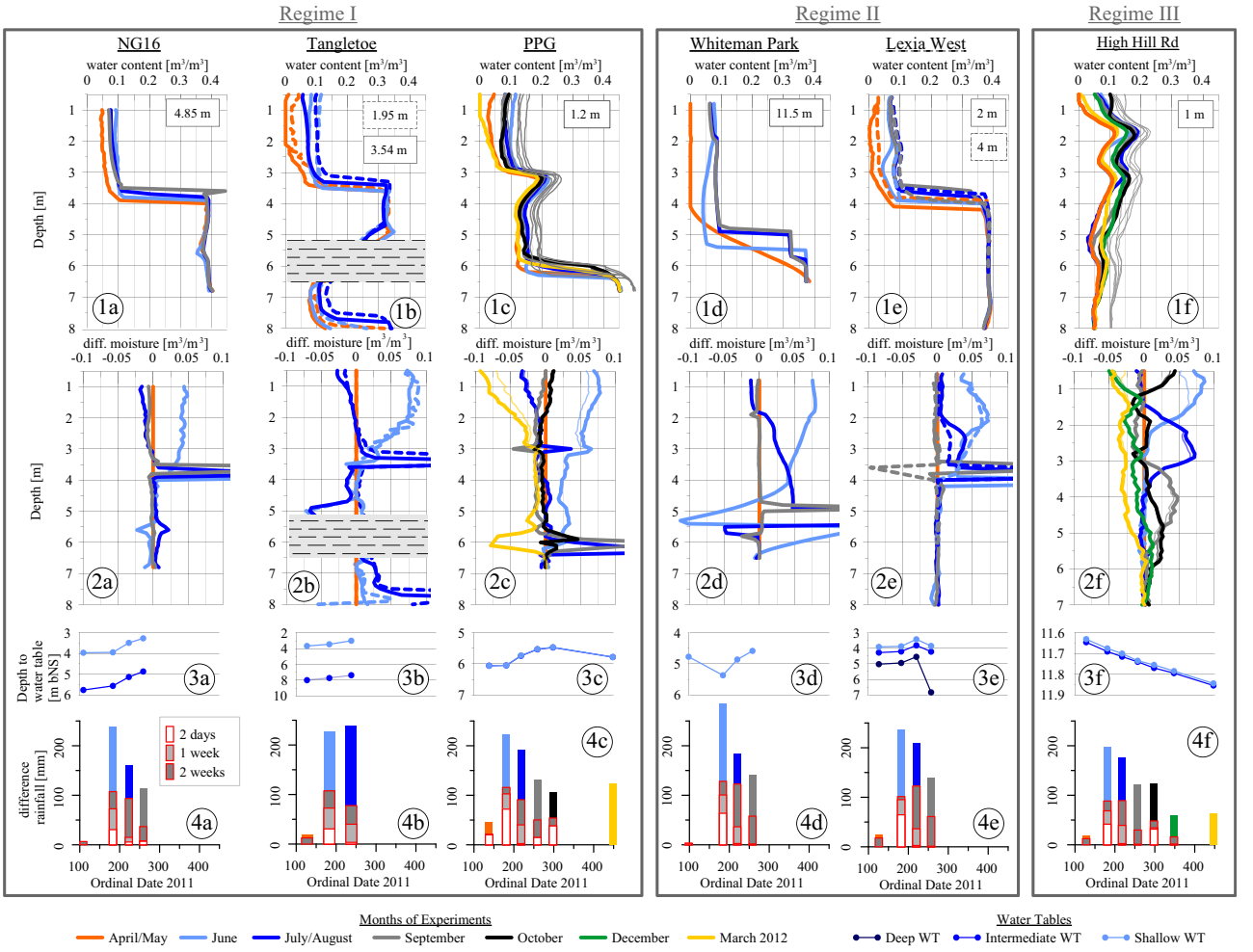

Figure 9. Compilation of ZOP results classified by infiltration Regimes I –III. Figures (1) are water content profiles (value in box indicates borehole separation), (2) sequential difference water content θ_s plots which show wetting (positive values) and drying (negative values) relative to the previous month, (3) are depth to water table values (dipper), and (4) rainfall charts of cumulative rainfall between subsequent repeats; cumulative rainfall before measurement are outlined in red filled in dark gray (2 weeks), light gray (1 week), and white (2 days). Note that all sites have very similar rainfall amounts before equivalent measurement days. Thin curves for PPG and HHW are curves before VRP matching, dashed curves for TGT and LXWA are for alternative well pairs (1.95 and 4 m separation, respectively).

(Figure 5). We found that high repeatability can be achieved for ZOP data based on similarity between saturated zone time-lapse curves (Figure 15) and repeats performed on 1 day (Figure 16).

Borehole separation has a profound impact on ZOP data. While larger borehole separation (i.e., approximately >5 m for 100 MHz antenna) reduces the errors associated with picking uncertainty and inaccuracy in borehole geometry, it leads to lower vertical resolution due to increased Fresnel zone and refracted energy can obscure low-velocity layers. Short borehole separation (i.e., <1.5 m) leads to high relative errors in travel time picking (i.e., for both, zero-time correction and first arrival picking) and potential near-field effects, whereas vertical resolution is not reduced. Note that a higher frequency antenna would be better suited for small well separations. However, in the following we will demonstrate that low frequency antenna (i.e., around 100 MHz) can still successfully be used in closed spaced wells using appropriate correction techniques.

Sites with larger well separation showed ZOP velocities that typically matched the VRP results but suffered from lack of vertical resolution (i.e., NG16, WP) [*Strobach et al*., 2012a, 2012b]. At site WP, refracted energy above and below the indurated sand horizon at 2 mbNS masks its low-velocity characteristic [*Strobach et al*., 2012a] and the ZOP velocity curves merely show a kink at the upper boundary of that horizon. Thus, the layer is not clearly resolved as a water-retentive (i.e., low-velocity) layer as described by *Bertuch and*

Froend [2006] and *Strobach et al*. [2011] (Figure 9, subfigure 1d). Critically refracted air-arrivals that appear in the data acquired close to the surface and at boreholes with large separation have very low amplitudes in comparison to the direct ground arrival. Interference with the direct arrival is therefore negligible. Independent slope analysis of the critically refracted airwave arrival as described by *Rucker and Ferre* [2003] largely corroborated the velocities obtained from direct ground arrivals.

NG16 has a high-velocity layer below the water table between 5.4 and 6 mbNS [*Strobach et al*., 2012b]. It is characterized by lower signal amplitudes, which could be explained by interference from a high-velocity (i.e., leaky) waveguide. Preliminary modeling predicts low amplitudes for ZOP data points within such a waveguide structure. The VRP data from NG16 [*Strobach et al*., 2012b] do not show great attenuation below this horizon thus indicating low losses (i.e., low electrical conductivity because of low clay content) and corroborating a geometric waveguide effect as the cause of attenuation. This leads us to conclude that higher velocity layers can be resolved despite large borehole separation because of refracted arrivals traveling along that horizon [*Strobach et al*., 2012a, 2012b], or a leaky waveguide effect.

LXAW and TGT have borehole pairs with different separations. At LXAW, the 2 m spaced boreholes Wa-Wb consistently show higher velocities compared to the well pair Wb-Wc which have 4 m separation (Figure 9, subfigure 1e). At site TGT conversely, we find that the well pair TGT_A and TGT_B (1.95 m separation) shows lower velocities when compared to TGT_A and TGT_C (3.54 m separation) (Figure 9, subfigure 1b). At both sites, VRPs are in favor of the higher velocity results. Thus, no consistent trend for ZOP results at different distances can be inferred from those sites.

HHW and PPG are sites with smallest well separation (0.98 and 1.17 m, respectively). While the vertical resolution of ZOP profiles appears higher than those of larger spaced boreholes, we had to improve repeatability and trueness at these sites. We noticed that time-lapse ZOP velocity curves did not match in the saturated zone after zero-time correction was applied for each month independently (Figure 6a). This mismatch coincided with unreasonable variations in the unsaturated zone velocities. While part of the unsaturated zone variation is due to increase in water content, the changes in the saturated zone are not expected. Possible reasons for mismatch are discussed in Appendix A and are related to the short well separation. Possible inaccuracies are due to error in zero-time determination, borehole geometry or near-field effects.

While using a higher frequency antenna or holes with larger separation can mitigate these problems, the necessary equipment or infrastructure is not always available. We now propose a workflow to improve the results obtained from closely spaced wells and low frequency antenna to obtain useful and high-resolution results. As saturated zone velocities are not expected to change, we calculate and apply a correction time for each repeat based on least-square minimization of travel time differences between measured data and the common average travel time in the saturated interval (Figures 6a and 6b). This lead to plausible unsaturated zone variations, and in the case of HHW the time-lapse velocities below 7 mbNS were largely identical except for slight changes in water table position. However, we noticed that ZOP velocity levels did not match the VRP results (Figure 6c). Thus, we further corrected ZOP velocities using a second constant time-correction to obtain a rough match in the unsaturated zone velocities of ZOP and VRP curves (below 7 m in HHW, and 4–5 m at PPG, Figures 6d, 7a, 7c, 8a, and 8b, dashed gray (uncorrected) versus colored (VRP matched)). Further discussion on accuracy, repeatability and the corrections we applied can be found in Appendix A.

4. Hydrogeologic Analysis and Implications

4.1. Time-Lapse Infiltration From Borehole Radar

For water infiltration analysis, two sets of temporal gradient curves are calculated from water content profiles obtained from ZOP measurements. The first type, $\theta_b(z)$, are difference to baseline moisture curves and represent changes in moisture content relative to the driest profile before rainfall (i.e., April or May data). An example is given as overlay in Figure 10. The integral

$$\Sigma S_{b,BHR} = \int_{z_1}^{z_2} \theta_b(z)\mathrm{d}z \tag{3}$$

over depth intervals [z_1 to z_2] of those difference profiles represents the cumulative storage $\sum S$ which is the cumulative water content change relative to the baseline month.

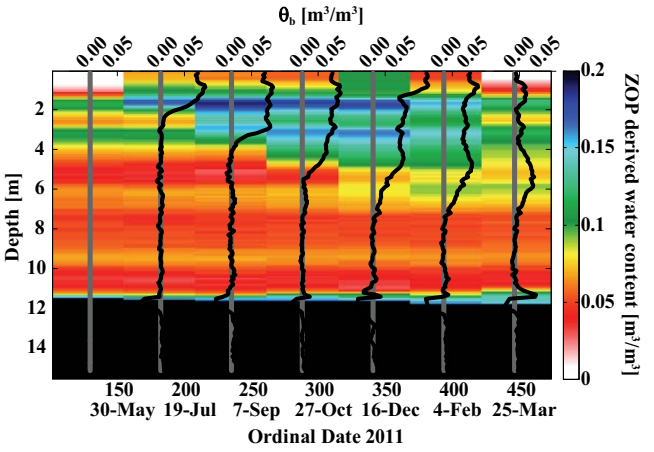

Figure 10. Pseudocolor plot of time-lapse water contents at HHW site where *x* axis represents time, and *y* axis depth. Line plots of baseline difference water contents θ_b depict the downward movement of the infiltration front.

The second type of gradient curves are sequential difference water content curves $\theta_s(z)$ obtained by calculating differences between successive moisture profiles (Figure 9, subfigures 2a–2f). Those curves can be useful to illustrate changes in water content between subsequent surveys. Positive values represent wetting, zero values no change and negative values drying. The integral:

$$\Sigma S_{s,BHR} = \int_{z_1}^{z_2} \theta_s(z)\mathrm{d}z \qquad (4)$$

over the unsaturated part of those sequential difference profiles provides directly information about the storage or loss of water in the soil relative to the previous month. This information can be useful for water balance calculation [*Sharma et al.*, 1991; *Farmani et al.*, 2008] and to detect the depth intervals at which changes occurred.

At most sites, wetting (increase in soil water storage) was observed on the second repeat at sites PPG, NG16, and TGT, and at the third repeat for sites WP and LXAW (Figure 9, subfigures 2a–2f). On the fourth repeat, in September, the sequential difference curves showed either no change, or drying. HHW is the only test site that showed different infiltration characteristics. At this site wetting occurred down to 7 mbNS and changes took place until October. In December, drying started above 5 mbNS while minimal wetting continued between 5 and 6.5 mbNS. The wetting during the first three measurements was delayed compared to all other test sites and thus we speculate that in 2011 only minimal or no recharge took place at HHW.

In order to compare test sites with each other, we consider unsaturated zone data that are present at all test sites (Figure 9, subfigures 1a–1f and 2a–2f). The limiting factor was therefore the depth to the shallowest water table, which was at TGT at a depth of 3.3 mbNS. Although this approach does not reflect the infiltration behavior of the total profile, it allows us to investigate the influence of retentive layers at shallow depth and enables comparison throughout all sites for overlapping dates.

HHW shows the highest overall water content within the interval 1–3.3 m due to the presence of two water-retentive layers (Figure 11a) and also has the greatest delay in wetting represented by wetting at the third repeat (see Figure 11b). Both, June and August cumulative sequential difference values show increased wetting of 0.072 m^3/m^2 (72 mm) and 0.085 m^3/m^2, respectively. The June difference for HHW is lower compared to the other sites despite similar rainfall in the period before the experiment (see Figure 9, subfigure 4f) which could be explained by water storage and loss in the first 1 m which is not accounted for in this graph. The high sequential moisture difference in August indicates a delayed wetting.

The infiltration behavior at the different sites leads to a classification based on wetting response to rainfall. *Regime I* is described by wetting of the full profile occurring after 200–250 mm of rainfall before June at sites PPG, NG16, and TGT (red, yellow and gray dots and lines in Figure 11). Further changes in unsaturated moisture could occur temporarily during infiltration events (e.g., HHW October 0–1 mbNS) or due to evapotranspiration. We believe that the initial wetting between first and second repeat produced a moisture content equivalent to the soils' field capacity.

Regime II is characterized by initial wetting of the profile whereas the upper 2 m are experiencing no more changes at the third repeat, while below 2 m there is a further increase in water content in August after another approximately 200 mm of rainfall (LXAW and WP, blue and green dots and lines in Figure 11). *Regime II* describes a delayed wetting response.

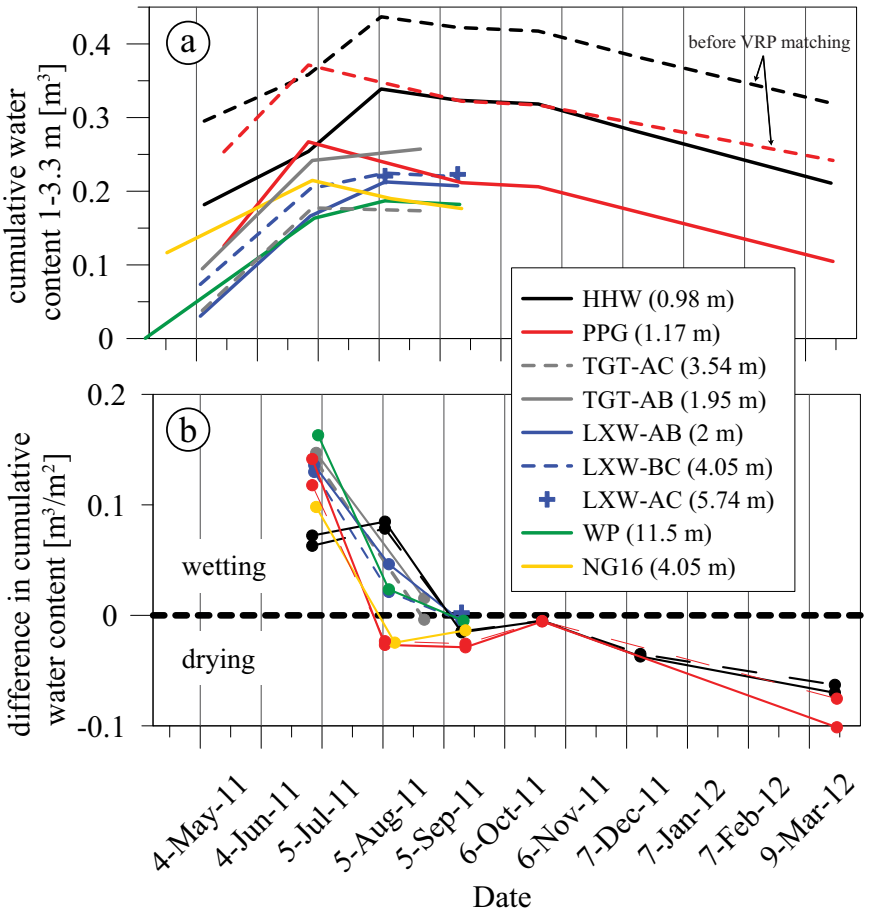

Figure 11. (top) Site-specific cumulative water content of depth interval 1–3.3 mbNS as a function of time (dashed black and red curves before VRP matching). (right) Temporal derivative of upper graphs, positive values stand for wetting, zero means no change and negative values drying. Values in bracket are borehole separation. Three Regimes are evident: (I) all changes at first repeat and no change or drying afterward (red, yellow, gray), (II) most change at first repeat, further change second repeat, afterward no change or drying (green, blue), and (III) some change at first repeat, same change second repeat, and no more change or drying afterward (black).

HHW represents *Regime III* with extremely delayed response and overall high water content due to the retentive soil layers in the upper 7 m (Figures 8a, 9f, 10, and black lines in 11).

The water content differences derived before VRP matching at HHW and PPG (dashed lines in Figure 11) show, that although the estimate of absolute cumulative water content in the soil profile is affected by the shift in velocity (Figure 11a), the sequential difference curves are less influenced by that inaccuracy (Figure 11b, also Figure 9, subfigures 2c, and 2f, faded versus bold curves). However, we believe that the shifted curves represent the actual velocities, and hence water contents, more closely than the initial estimates.

4.2. Toward a Water Balance Evaluation

As described above, we assume that negligible amounts of water reached the water table at the HHW test site in 2011. In that case, a water balance can be calculated (Figure 12). The simplified water balance equation for the case of no flux to the water table and neglecting runoff from or to the site can be written as [*Scanlon et al.*, 2002]:

$$P = ET + \Delta S \tag{5}$$

with P the precipitation, ET evapotranspiration, and ΔS the water storage in the soil. Quantities are typically given as rates in millimeter per time interval. For our calculations, we chose the time interval according to the days between subsequent field experiments. ΔS_s is the sequential water storage in the soil calculated

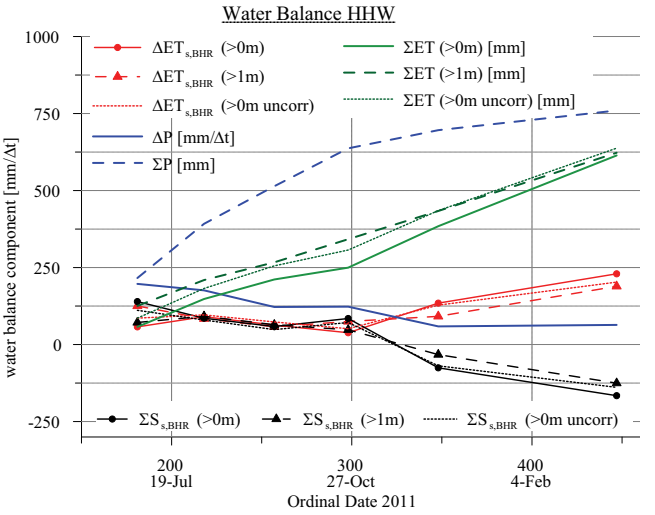

Figure 12. A water balance calculation for HHW under the assumption of negligible flux below 7 mbNS. Sequential difference evapotranspiration estimates $\Delta ET_{s,BHR}$ are given for the unsaturated zone from 0 to 11.5 mbNS (solid red line and dots) and 1 to 11.5 mbNS (dashed red line and triangles) and also for the unshifted ZOP data (dotted red line). Cumulative storage $\sum S_{s,BHR}$ is plotted in black. Note the cumulative evapotranspiration estimate $\sum$ ET for shifted and unshifted ZOP results (green solid and dotted lines, respectively) yield similar values of 614 and 637 mm, respectively. For a full wetting-drying cycle including drying in April/May 2012, the balance is expected to converge.

based on equation (4). Note that we extrapolated data from 1 mbNS to zero depth because we found that the missing interval would have a great influence on evapotranspiration estimates as evident in Figure 12. This figure also shows the results of the uncorrected ZOP data, which initially overestimates total evapotranspiration due to underestimating the change in stored water in the unsaturated soil. However, the cumulative annual evapotranspiration is almost identical to the corrected curves. While wetting periods are overestimated by uncorrected velocities, the drying periods are equivalently underestimated. For annual evapotranspiration which includes wetting and drying we can therefore conclude that the accuracy of absolute water content in the profile is even less important than for sequential difference curves. The overall evapotranspiration estimated from the ZOP experiments is 620 mm which compares well with values found in the literature. *Farrington et al.* [1989] derived 666 mm annual evapotranspiration with annual rainfall of 865 mm at similar Banksia woodland vegetation. *Sharma et al.* [1991] indirectly find evapotranspiration values with the zero flux plane technique between 600 and 700 mm for different test sites with annual precipitation of 740 mm. Note that our measurements did not span a full year and some evapotranspiration would have been expected for the months April and May.

4.3. Discussion on Infiltration Observation

We argue that by correcting initial ZOP velocity estimates to VRP velocity levels, we can increase the certainty of the water content estimate because VRP should provide better trueness. While the applied correction has a great influence on absolute water content, the influence on sequential difference curves is minor as will be shown by the following examples.

The sequential difference curves derived for corrected and uncorrected ZOP water content estimates at HHW and PPG differ in that the uncorrected curves show smaller variation in water content difference between subsequent measurements (Figure 9, subfigures 2c, and 2f, thick (corrected) versus thin (uncorrected)). However, the impact of the correction does not influence the qualitative interpretation of those curves. From cumulative sequential difference curves obtained from the corrected and uncorrected ZOP data for the entire unsaturated zone at HHW and PPG, it can be seen that stored soil water values only vary by a few millimeter, with a maximum of 40 mm for the first repeat at PPG (Table 2). Sequential soil moisture estimates are not sensitive to velocity correction for the limited depth interval 1–3.3 mbNS (Figure 11, lower, solid (corrected) versus dashed (uncorrected)). Thus, determination of sequential change of moisture is not very sensitive to absolute moisture content.

However, sequential difference values are sensitive to noise and imprecision. The good repeatability that was achieved for ZOP data by saturated zone matching is therefore critical for baseline and sequential difference analysis. The same general statements are true for neutron, or any other type of time-lapse data.

Another aspect that deserves mentioning is the limitation of having only few repeats, for example, at TGT where a baseline measurement was followed by two repeats. From the data, we can deduce that the initially dry or slightly moist unsaturated zone experienced major wetting after approximately 230 mm rainfall

Table 2. Sequential Difference of Soil Water Storage Values Derived From Time-Lapse ZOP Experiments and Cumulative and Sequential Difference of Rainfall During Study Period[a]

		High Hill Road West (HHW)	North Gnangara, Airfield Road (NG16)	Lexia West (LXWA)	Whiteman Park Site 4 (WP)	Pinjar Piggery (PPG)	Tangletoe Swamp (TGT)
Weather Station		Gingin Aero	Gingin Aero	WP	WP	Mariginiup	Gingin Aero
Precipitation P							
Measurement							
First	ΣP (mm)	19	7	25	3	46	19
Second	$\Sigma P/\Delta P_s$ (mm)	216/197	246/239	261/236	288/285	269.4/223	246/227
Third	$\Sigma P/P_s$ (mm)	392/176	407/161	471/210	471/183	460/191	484/239
Fourth	$\Sigma P/P_s$ (mm)	514/122	521/114	611/140	612/141	591/131	
Fifth	$\Sigma P/P_s$ (mm)	637/123				697/106	
Sixth	$\Sigma P/P_s$ (mm)	696/59					
Soil Water Storage S							
Second	$\Delta S_{s,BHR}$ (mm)	140[b] (111)[b,c]/72 (63)[c]	98	136 (130)[c]	163	275[b] (236)[b,c]/142 (118)[c]	147 (139)[b]
Third	$\Delta S_{s,BHR}$ (mm)	86[b] (80)[b,c]/85 (79)[c]	−25	46 (21)[c]	24	−63[b] (−56)[b,c]/−27 (−23)[c]	15 (−4)[b]
Fourth	$\Delta S_{s,BHR}$ (mm)	59[b] (49)[b,c]/−15 (−15)[c]	−14	−5 (−5)[c]	−5	−53[b] (−49)[b,c]/−29 (−26)[c]	
Fifth	$\Delta S_{s,BHR}$ (mm)	85[b] (72)[b,c]/−5 (−5)[c]				−3[b] (−4)[b,c]/−6 (−5)[c]	
Sixth	$\Delta S_{s,BHR}$ (mm)	−76[b] (−69)[b,c]/−37 (−35)[c]					
Seventh	$\Delta S_{s,BHR}$ (mm)	−166[b] (−139)[b,c]/−70 (−63)[c]				−226[b] (−177)[b,c]/−101 (−75)[c]	

[a] ΣP: cumulative precipitation P, ΔP_s: sequential difference of P, $\Delta S_{s,BHR}$: sequential difference of S.
[b] Values for full unsaturated zone.
[c] Unshifted ZOP results (HHW, PPG) or alternative well pair (TGT_{AC}, $LXWA_{BC}$).

with 20 mm within the 2 days preceding the first repeat. Because of the second repeat 1 month later and after another 240 mm precipitation reveals drier conditions in the near-surface and no change between 1.4 and 3.3 mbNS, it is likely that the soil was already at field capacity the previous month, and possibly slightly above field capacity above 1.4 mbNS due to the rainfall shortly before the measurement. As other sites confirm this behavior, it is reasonable to conclude that only three measurements were sufficient to characterize the preinfiltration soil conditions, and that field capacity was reached at the latest after 230 mm of rainfall. Sparsely sampled soil moisture development does in this case not allow to characterize the unsaturated hydraulic conductivity, or to deduce a water balance. For this, frequent repeats on an hourly or daily basis are necessary to record the movement of an infiltration plume through the prewetted soil to determine infiltration velocity.

To evaluate the soil moisture variations in a hydrogeologic sense, we now discuss how basic environmental factors evident on the surface may relate to the observed infiltration characteristics. Key components are vegetation (i.e., type and abundance) at the site (i.e., water input between subsequent experiments and immediately before the experiments) (Table 1), cumulative rainfall (Table 2 and Figures 9, subfigures 4a–4f) and near-surface soil properties (Table 1 and Figure 2).

Regime I was identified at sites where vegetation was either absent (NG16, PPG) or reduced (TGT). Infiltration appears to be rapid as the sands are likely still moist from the previous winter. Soil evaporation, that is evaporation from solar irradiance and heating of the shallow subsurface without the influence of vegetation, does not reach depths of more than approximately 0.5–1 m. The water content at field capacity below approximately 1 m is therefore not lost during the summer time. Thus, soils are prewetted when the first rain falls, and water will quickly drain and elevate water contents above field capacity. Due to the long times between sampling, a period of approximately 1 month, more detailed interpretation is not possible.

Regime II sites had intact native vegetation (WP, LXAW). The prewetting of the unsaturated zone below 2 m depth in June can be explained by preferential flow. Before the main wetting front penetrates the full profile, flow will be channeled along pathways predefined by roots, hydrophobic sand, and burrows. As a result, the soil moisture distribution is predicted to be inhomogeneous. The measured water contents are lower compared to those observed once the main wetting front completely saturates the remaining dry volume in August. A second explanation for delayed infiltration is the cemented, indurated sand horizon at WP between 1.7 and 2.3 mbNS. In this case if the cemented surface has some dip, it might function as a capillary barrier and flow might be directed out of the crosswell radar plane between the wells. *Strobach et al.* [2010b] found indications of dipping layers at several locations at the Gnangara Mound.

At LXAW, no distinct horizon is evident, neither from drill reports [*McHugh*, 2011] nor from the GPR signature. However, the near-surface properties could also explain the delayed wetting. The LXAW site is at the

outskirts of the Lexia wetland complex and on the surface is a layer rich in organic material. This layer can likely store water in the very near surface as observed at another wetland by *Strobach et al*. [2013] that may evaporate after rainfall and explain delayed wetting.

Regime III at HHW is a combination of a vegetated test site and several indurated and cemented soil horizons. Neutron logging and VRPs from the two adjacent holes indicate that the first few meters contain several water-retentive layers. Their position is generally shallower in well Wb compared to Wc which indicates dipping structures. Surface common offset GPR confirms that observation. It is therefore possible that preferential flow follows the dips as proposed in *Strobach et al*. [2010b]. The top soil layer is also rich in organic material, which is likely a remnant from a previous wetland in that area [*Searle and Bathols*, 2009]; thus, making surface runoff to the adjacent sand track possible. At this site the water table did not rise (see Figure 9, subfigure 3f). Thus, there was no seasonal recharge at this area. In fact, the water table declined by 20 cm. Whereas all the other sites showed an increase in local water table elevation, which is consistent with recharge from infiltration [*Scanlon et al*., 2002]. The neutron data support the hypothesis of no recharge in some years for a similar site as previously discussed.

5. Conclusions

Borehole radar techniques were successfully deployed for time-lapse monitoring of rainfall infiltration into a layered sandy soil during an annual recharge cycle in Mediterranean climate. Zero vertical offset crosswell profiling ZOP and vertical radar profiling VRP measurements were performed on a monthly basis. Soil moisture profiles reveal infiltration characteristics of six test sites located on the Gnangara Mound, north of Perth, Western Australia. High repeatability in the saturated zone proves that ZOPs can provide high precision velocity profiles.

To obtain reliable water content profiles from ZOP measurements, we had to overcome initial problems. We found that the initial absolute velocity estimates derived from in-hole radar travel times for shortly spaced wells exhibit poor repeatability, likely associated with zero-time correction inaccuracies. However, we were able to correct zero-time inaccuracy based on matching travel times in the saturated zone for which saturation and travel time are expected to be constant. Larger discrepancies between VRP and ZOP velocity estimates were observed at sites with small well spacings. Explanations for that inconsistency are inaccuracies in well separation or borehole deviation, high uncertainty in zero-time correction and near-field effects, all of which are less influential on VRP velocity calculation based on local slopes. Hence, the zero-offset VRPs provide a robust, independent estimate of interval velocity that can be used to correct ZOP results (i.e., to improve their trueness). Those matching techniques provide a workflow for correcting ZOP data for closely spaced wells. For larger well separation, the obtained accuracy is sufficient and the matching was not necessary. However we note that refracted energy and an increased Fresnel zone can reduce vertical resolution of ZOP measurements if the distance between wells is too large. This is especially true where high dielectric permittivity (i.e., low-velocity) layers exist within a low dielectric permittivity (i.e., high-velocity) background.

Data analysis based on VRP data alone is challenging as VRPs show lower long-term repeatability as determined from monthly time-lapse data (see Appendix B), and analysis may suffer from interference with upgoing wavefields leading to extreme slope estimates. On the other hand, VRPs may provide higher vertical resolution than ZOPs because refracted energy is absent. VRPs can further provide valuable information for surface GPR such as estimates of signal attenuation, subsurface layering and layer reflectivities. While our work clearly indicates that time-lapse ZOPs provide high repeatability, we would strongly recommend measuring VRPs with ZOPs to have an independent interval velocity, and the additional information content of the full waveform from the VRP data.

The time-lapse moisture curves derived from crosswell ZOP measurements revealed different infiltration characteristics for the different test sites. We identified three regimes. Regime I shows simple infiltration behavior where the initially dry unsaturated zone in May is transformed into a wet soil at its field capacity after approximately 200 mm of rainfall in June/July. Regime II is characterized by initial prewetting in June/July and saturation to field capacity after approximately 400 mm precipitation in August. One site showed no change in the unsaturated zone below 7 mbNS and was categorized into infiltration Regime III. Although flow could have still occurred [*Scanlon et al*., 2002; *Sharma et al*., 1991], time-lapse neutron data from a

similar site confirms that large flux is likely to increase the water content even at greater depth. The falling water table further indicates that only minimal or no recharge occurred from the winter rainfall cycle in this area. We calculate the water balance to get an estimate of evapotranspiration and obtain a cumulative value of 620 mm for the 10 month observation period (84% of total precipitation).

A comparison between time-lapse neutron logging and crosswell radar data reveals highly comparable infiltration behavior.

Advantages of crosswell radar are: (i) deployment risk is negligible compared to neutron methods involving radioactive sources, (ii) measurements represent a larger volume of earth compared to repeat logging in a well, (iii) calibration to water content is robust for simple soils. The in-hole radar acquisition and processing scheme (i.e., VRP and ZOP) we have presented provides practitioners with a robust tool for obtaining time-lapse infiltration information for estimating hydraulic properties of the unsaturated zone which can in turn reveal infiltration mechanisms and ultimately lead to an estimated water balance.

Appendix A

Time-lapse neutron logging data from previous years acquired at nearby sites provides information on infiltration behavior independent of the GPR investigations. Neutron data that is available for a test site PV3 that is approximately 3 km to the southwest of HHW, and the Whiteman Park site 4 (Figure 1, blue circles). Data were collected for Water Corporation between 2002 and 2004 at PV3, and between 2009 and 2011 at Whiteman Park for Ray Froend from Edith Cowen University [*Froend et al.*, 2010] (see Figure 4). PV3 site characteristics are similar to HHW site with two indurated sand intervals and a deep water table. At WP, the neutron data have been acquired in the same borehole as the crosswell BHR. Data were collected by Kel Baldock with a Didcot neutron probe that uses an Americium-Beryllium fast neutron source. Measurements were performed at a vertical depth interval of 0.25 m with a measurement duration of 16 s per depth point. Time-lapse experiments were performed on a monthly or bi-monthly basis. The neutron data presented is in units of raw counts (Figures 13a and 14a). Calibrations to obtain water content are not available, however, the water content versus neutron count relationship is typically linear [*Bell*, 1987]. Values between 20 and 60 counts represent dry sections with water contents around 5 vol%. Full saturation (i.e., 30–40 vol%) shows counts around 350–400. The expected field capacity of the sands is at approximately 8–10 vol% water content, and therefore at counts around 80–100.

For the purpose of this comparative study, relative changes in neutron counts with time reveal the mechanisms of recharge. We treated the raw time-lapse neutron count profiles identically to the BHR data in that we calculated sequential difference curves that we call ΔN^s. The resulting sequential difference curves are shown for winter months of 2009 and 2010 at Whiteman Park in Figures 13b and 13c, respectively; and for PV3 (Pinjar area) for years 2002 and 2003 in Figures 13b and 13c, respectively. Raw neutron data were gridded to obtain regular time intervals as shown in Figures 13a and 14a for sites WP and PV3, respectively. Black vertical lines indicate dates of measurements. We were able to identify the same infiltration regimes in the neutron data that were derived from the GPR study. While a calibration to absolute water contents would be desirable, the raw counts still show how recharge is influenced by climatic and soil conditions.

The WP neutron data confirmed the GPR interpretation and Regime II as shown in Figure 13. In both years, 2009 and 2010, there was a slight delay in infiltration below the cemented soil horizon. We note that the winter of 2010 had exceptionally low rainfall with annual precipitation of 470 mm (Whiteman Park climate station, http://www.bom.gov.au/climate/data/), while 2009 was an average year with almost 700 mm (Figure 4). The neutron data reveals lower neutron counts in 2010 compared to 2009 which indicates that the water balance within a thin vadose zone of less than 4 m is influenced by variations in rainfall.

The test site PV3 close to HHW has an extensive vadose zone with deep water table. Figure 14a reveals a water-retentive soil horizon at around 4.5 mbNS and between 9 and 12.5 mbNS. We observe that 2002 was an extremely dry year with rainfall of 491 mm (Gingin Aero climate observatory, http://www.bom.gov.au/climate/data/), that was preceded by a sequence of below average rainfall years 2000 and 2001 (636 and 572

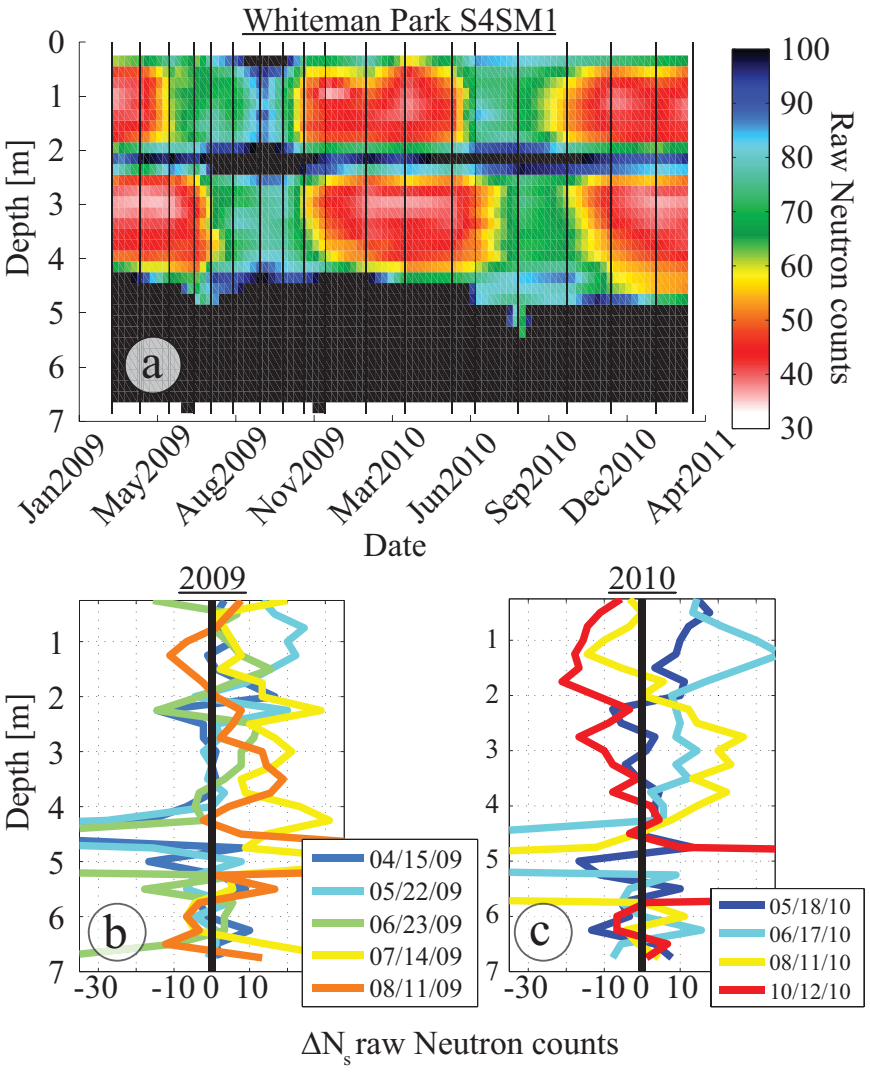

Figure 13. Pseudocolor time-lapse representation of raw neutron counts from WP, measurement dates are indicated by black vertical lines in Figure 13a. Sequential difference curves of wetting cycles from 2009 to 2010 are shown in Figures 13b and 13c, respectively. In Figures 13b and 13c, positive counts represent wetting and negative counts drying. Both years show delayed wetting below the water-retentive horizon at 2 mbNS, equivalent to Regime II.

mm/a, respectively). The following year 2003 was slightly wetter with 680 mm. The infiltration characteristics at PV3 are very similar to what we observed at HHW. The wetting front gradually moves downward as depicted in Figures 14b and 14c. Below 12 m no changes are obvious in 2002/2003 (Figure 14b), and neutron counts within that depth interval are generally low (65–75). Although it could be argued that the soil is already at its field capacity and no more wetting can therefore be expected, the 2003/2004 data show how the wetting front moves further and elevates the soil moisture to what we believe to be slightly above the soil's field capacity between 12.5 and 17 mbNS (Figure 14c). It is unlikely that major downward movement of water took place in 2002/2003 since one would expect that the soil's matrix potential would attract some of the passing water as observed in 2003/2004. *Scanlon et al.* [2002] points out that the interpretation of no-flow based on lack of change in moisture content is often incorrect as unsaturated flow at field capacity or even slightly below is possible. In our case, however, the changes of the subsequent year indicate that the movement of the infiltration front considerably increases the soil moisture at depths below 12.5 m at this site. The migration of water to depths beyond 12 m is delayed in 2003/2004 and the infiltration front finally reaches the water table in February 2004. The last measurement in September 2004 shows that the moisture between 12.5 and 16.5 mbNS returns to values around the soil's field capacity.

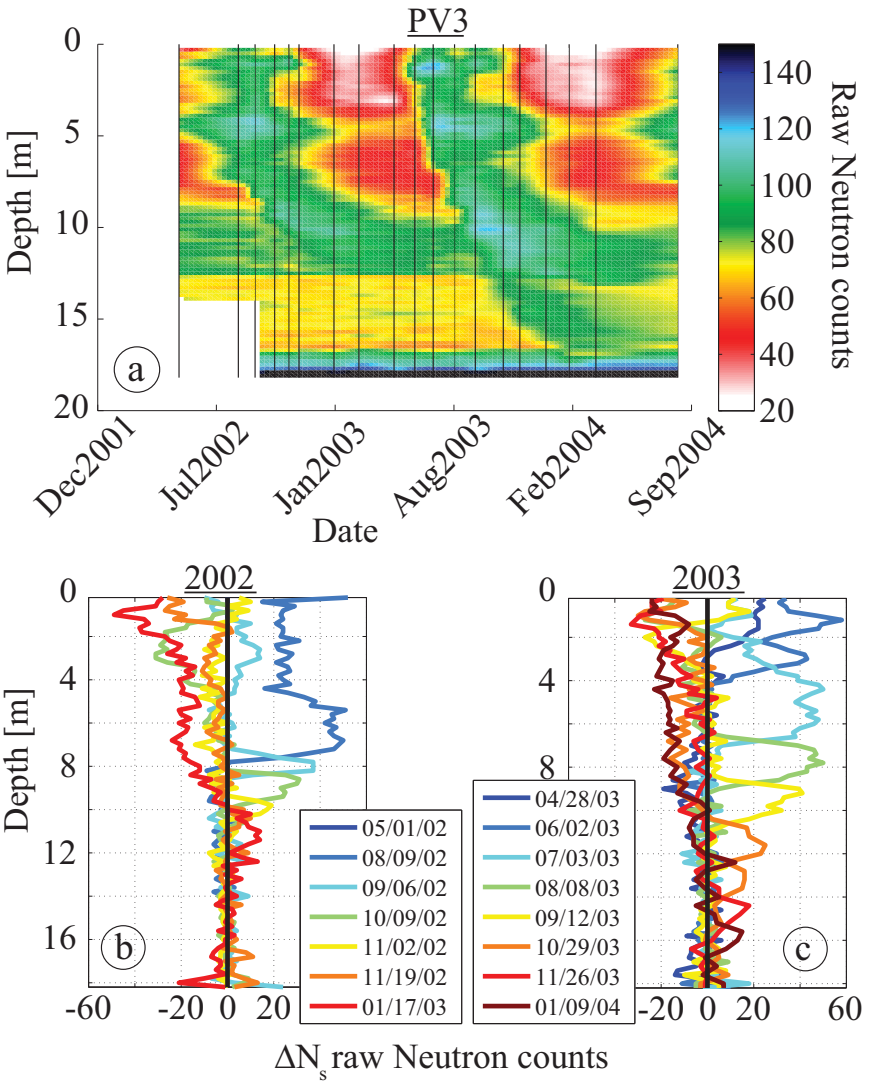

Figure 14. Pseudocolor time-lapse representation of raw neutron counts from PV3 measured at dates indicated by black vertical lines (a) and sequential difference curves of wetting cycles from 2002 to 2003 in Figures 14b and 14c, respectively. In Figures 14b and 14c, positive counts represent wetting, while negative counts drying between subsequent measurements. Both years show delayed wetting below the water-retentive horizons at 4.5 mbNS equivalent to Regime II, and severely delayed wetting below retentive horizon between 9 and 13 mbNS in 2003, and no changes below that horizon in 2002 (Regime III). Note that measurements in 2002 started in May and first repeat was in August, while in 2003, measurements were done every month between April and November. Hence, the sequential difference curves represent change between different lengths time intervals.

Appendix B

Precise recovery of subsurface properties from BHR can be problematic and care has to be taken to avoid artifacts and false velocity estimation [*Peterson*, 2001]. Phenomena such as energy traveling from antenna tip to tip at high ray angles [*Irving et al.*, 2007], variation of zero-time [*Peterson*, 2001], borehole deviation, waveform distortion, and refracted energy [*Rucker and Ferre*, 2003; *Tronicke and Knoll*, 2005] can lead to under or overestimation of true ground velocity.

In the following, we will use a terminology where precision and repeatability are synonymous and largely describe how reproducible results are for measurements in quick succession and after saturated zone matching procedure (i.e., no environmental time-lapse changes while long-term instrumental drift is corrected). Trueness describes the absolute correctness of obtained values relative to a reference measurement (or the real value if known), and both, repeatability and trueness determine accuracy.

Repeatability is determined by the BHR instrumentation, experimental procedure, and data analysis approach, and it is generally high for BHR measurements. Short-term instrument drift can be a source of imprecision as zero-time corrections change within the duration of an experiment [*Peterson*, 2001]. Due to the short duration of our experiments (i.e., smaller one minute), instrument drift is not expected, which is confirmed by measurements in air before and after acquisition, and as well by the repeatability obtained in the saturated zone (Figure 15) and for quick successions at HHW (Figure 16). However, the repeats performed in the same wells and the same day show that some long-term instrument drift is evident. However, this change in zero-time is correctable by for example saturated zone matching. Thus, high repeatability can be achieved for long-term time-lapse ZOP measurements in case data from an interval that does not experience changes between repeated measurements is available (e.g., saturated zone, see Figure 15). *Alumbaugh et al.* [2002] investigate precision from repeatability of multioffset crosswell BHR tomography experiments and obtain an average RMS precision error (i.e., standard deviation) of 0.54 ns. Their methodology, however, does not provide an independent estimate for ZOPs. For saturated zone time-lapse ZOPs (see Figure 15), we recovered average standard deviation values of 0.082 ± 0.037 ns (0.00018 ± 0.000087 m/ns) at LXAW and 0.113 ± 0.061 ns (0.00022 ± 0.00013 m/ns) for TGT (error values are average standard deviation of each depth level). The high repeatability of ZOPs could not be matched by VRPs. Interfering wavefields, imprecise picking, and lower S/N are reasons for lower precision. At PPG, we determined repeatability from the saturated zone time-lapse results by calculating standard deviation of velocity for each

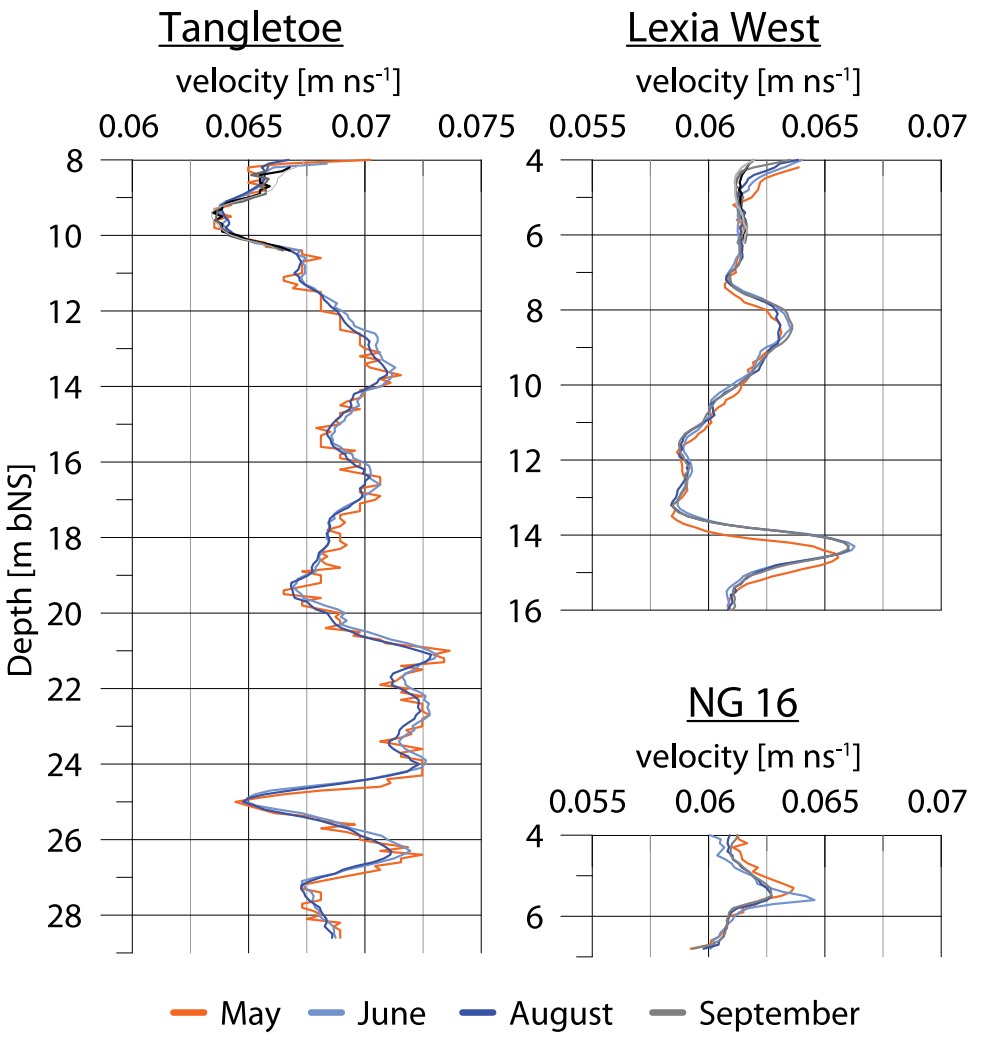

Figure 15. Time-lapse zero-offset crosswell radar velocity profiles for the saturated zones at three sites demonstrate high repeatability after matching procedure has been performed as explained in the text. Only at Lexia West we observed a vertical shift in the May data that was caused by triggering errors of the acquisition system.

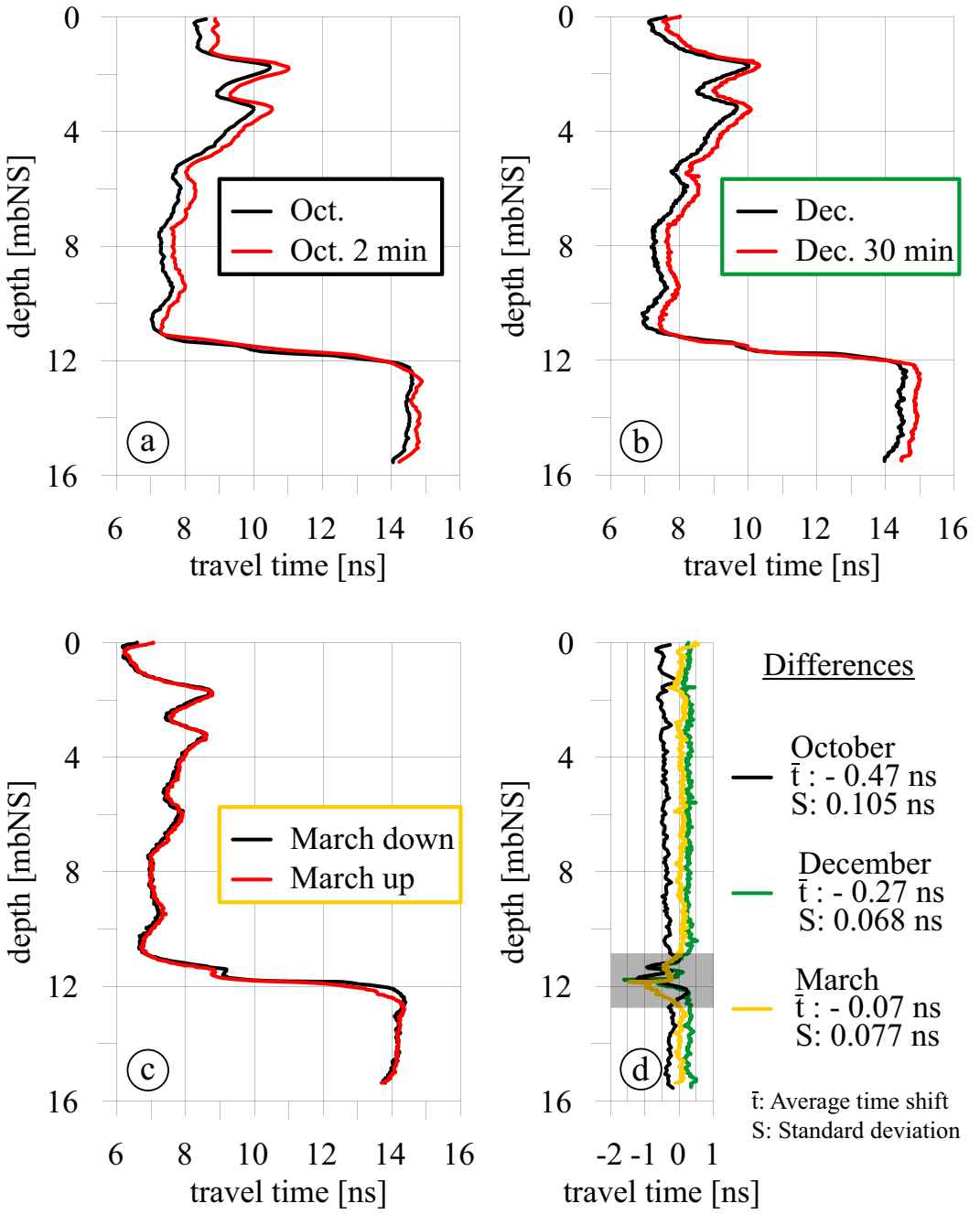

Figure 16. ZOP measurements repeated in short succession (i.e., (a) after 2 min, (b) after 30 min, (c) up-hole measurement immediately after down-hole) and in the same crosswell configuration. (d) The difference between subsequent runs. Note that data in grey shaded box in Figure 16d has been omitted for calculation of average and standard deviation. Average time shift is equivalent to trueness, the standard deviation represents (corrected) repeatability.

depth interval and obtain an average value of 0.0034 ± 0.0014 m/ns). As discussed in the main text, the trueness of absolute velocities is probably accurate within their precision error because slope analysis of first arrivals is independent of zero-time correction and associated systematic errors. This is also evident from the fact that time-lapse curves scatter around their mean and do not show systematic shifts as the ZOP data does. Another advantage of VRPs is that temporal variation of zero-time has a small effect on VRP slopes, and variations due to changes in antenna coupling with different lithologies only produces inconsistencies at the interface but not within formations.

The trueness of measured ZOP interval velocities depends on the physics of EM wave propagation in an inhomogeneous medium, and the method applied to extract absolute travel times and to calculate interval velocities. Trueness and resolution of BHR is on a first order controlled by (i) zero-time correction (t_{corr}) and picking accuracy; (ii) borehole separation (i.e., large separation → long travel time → less effect of poor trueness in t_{corr} and picking) and accuracy of borehole geometry (e.g., possible unknown deviation); (iii) material dielectric properties (i.e., high dielectric permittivity → greater travel time; → higher accuracy in saturated than unsaturated zone); (iv) measurement frequency and antenna properties (i.e., higher frequency → smaller antennae and shorter wavelengths → higher resolution and more accurate picking); (v) wavefield and propagation stability (i.e., interfering wavefields, refracted energy, dispersion, lossy materials, and waveguide effects); and (vi) direction of measurement relative to anisotropy (e.g., parallel or perpendicular to layering). Some of the aspects above are contrary to each other, for example, larger borehole separation results in smaller travel time errors in regards of picking and zero-time correction, but also leads to refracted energy and hence overestimation of interval velocity and loss of layer resolution. Near-field effects can introduce further complication in crosswell BHR. For a center-fed dipole (i.e., borehole antenna) of length D, the reactive near-field is dependent on the wavelength λ and extends to $R_{ReacNF} = 0.62\sqrt{\frac{D^3}{\lambda}}$ and the radiating near-field to $R_{RadNF} = 2\frac{D^2}{\lambda}$ [*Balanis*, 1982]. According to these equations, for a 1.5 m long dipole antenna with a center frequency f of 100 MHz $\left(\lambda = \frac{v}{f}\right)$, the reactive near-field is between 0.9 and 1 m for unsaturated velocities between 0.15 and 0.13 m/ns, respectively, and between 1.35 and 1.5 m for saturated velocities between 0.07 and 0.06 m/ns, respectively. Measurements in the unsaturated zone at HHW and PPG are at the boundary between reactive and radiating near-field, and clearly within the reactive near-field for the saturated zone. Changes in subsurface properties shift the near-field boundaries which has implications for time-lapse investigation in the unsaturated zone. Inconsistencies can be a result, and only a good understanding and a correction of the effect of near-field measurements on recorded waveform can mitigate these inconsistencies. The quantitative effect of performing measurements in the near-field of a center-fed dipole has not been described for BHR in the literature, and is beyond the scope of this work. Another alternative to avoid near-field problems is to use a higher-frequency antenna.

The trueness in tomographic BHR (e.g., ZOP) can be poor due to systematic errors in zero-time determination. To have consistency throughout the data sets, we initially used zero-time corrections from a constant air separation of 3 m and travel time determined from the zero-crossing. The estimated accuracy of the resultant zero-time correction is between 0.5 and 1 ns. Velocity calculation is directly influenced by zero-time correction. Depending on the absolute travel time (i.e., ground velocity and borehole separation), the influence of inaccurate zero-time can be large. For example, boreholes with 1 m separation and a ground velocity of 0.13 m/ns record a travel time of 7.7 ns and an error of ± 1 ns results in velocity estimates between 0.115 and 0.149 m/ns, an unacceptable result, but realistic for low-frequency crosswell BHR.

At HHW, we observe a further mismatch that is concerned with saturated and unsaturated velocities. After shifting the ZOP curves to the VRP level, the saturated velocities appear too large. In *Strobach et al*. [2012a, 2012b], we find various explanations for that phenomenon. One reason could be deviating wells, which would lead to larger velocity estimate in case of decreasing well separation, or underestimation of velocity for increasing well separation. A second explanation is near-field effects (i.e., unsaturated zone is in radiating near-field and saturated zone in reactive near-field).

We used the VRP results to increase trueness of ZOP measurements. However, an alternative explanation for observing different velocities from VRP and ZOP measurements is anisotropy. In case VRPs record higher velocities, the vertical velocity is higher than the horizontal velocity. In a depositional soil environment, however, horizontal layering would lead to higher horizontal velocity which contradicts the observation. On the other hand, hydrophobic patches or preferential flow paths may produce vertical high- or low-velocity channels, respectively. However, further research is required to determine the cause of saturated-unsaturated zone mismatch.

Furthermore, the trueness of water content estimation is dependent on the certainty of the mixing model or empirical relationship used to convert velocities to volumetric water content. Ideally, a relationship between dielectric permittivity and volumetric water content is established for every stratigraphic unit or soil horizon. Note that we measured this relationship for representative samples of clean sand and indurated sand in a coaxial transmission line and found that the empirical Topp relationship [*Topp et al*., 1980]

fitted the data within its error bounds [*Strobach*, 2013]. We believe that measurement errors related to the inaccuracies described above outweigh the error related to water content conversion.

Acknowledgments
Majed Almalki, Eva Caspari, David Euteneuer, Andrew Greenwood, Franka Menzel, Konstantin Tertyshnikov, and Sinem Yavuz assisted with the data collection in the field. Elmar Strobach is supported by a CIPRS scholarship through Curtin University and an ASEG research foundation grant. Groundprobe Ltd. kindly provided the borehole radar antennae. Ray Froend and Muriel Davies provided soil information and direct moisture content measurements at Whiteman Park. Kel Baldock measured and provided the neutron data. Data can be obtained from the corresponding author free of charge upon request. The manuscript was improved by a constructive review process. We appreciate the ongoing support from both the Water Corporation and DoW, who make significant contributions to hydrogeophysical research and development.

References

Alumbaugh, D., P. Chang, L. Paprocki, J. Brainard, R. Glass, and C. Rautman (2002), Estimating moisture contents in the vadose zone using cross-borehole ground penetrating radar: A study of accuracy and repeatability, *Water Resour. Res.*, *38*(12), 1309, doi:10.1029/2001WR000754.

Balanis, C. (1982), *Antenna Theory: Analysis and Design*, 2nd ed., John Wiley, New York.

Bell, J. (1987), *Neutron Probe Practice*, 3rd ed., *Tech. Rep. 19*, Inst. of Hydrol., Wallingford, U. K.

Bertuch, M., and R. Froend (2006), Winter drawdown trial—Whiteman park, soil characterisation report, technical report, Edith-Cowan Univ., Sch. of Natl. Sci., Perth, Australia.

Binley, A., P. Winship, R. Middleton, M. Pokar, and J. West (2001), High-resolution characterization of vadose zone dynamics using cross-borehole radar, *Water Resour. Res.*, *37*(11), 2639–2652.

Brovelli, A., and G. Cassiani (2008), Effective permittivity of porous media: A critical analysis of the complex refractive index model, *Geophys. Prospect.*, *56*(5), 715–727.

Buursink, M., J. Lane Jr., W. Clement, and M. Knoll (2002), Use of vertical-radar profiling to estimate porosity at two New England sites and comparison with neutron log porosity, in *Proceedings of SAGEEP*, vol. 2, Denver, Colorado., Environmental and Engineering Geophysical Society, CD-ROM, 12 pp.

Cassiani, G., N. Fusi, D. Susanni, and R. Deiana (2008), Vertical radar profiles for the assessment of landfill capping effectiveness, *Near Surf. Geophys.*, *6*, 133–142.

Chang, P.-Y., D. Alumbaugh, J. Brainard, and L. Hall (2004), The application of ground penetrating radar attenuation tomography in a vadose zone infiltration experiment, *J. Contam. Hydrol.*, *71*(1–4), 67–87, doi:10.1016/j.jconhyd.2003.09.011.

Cox, M., M. Preda, and J. Harbison (2002), Importance of indurated sand layers to groundwater flow in quaternary coastal settings, Moreton bay, in *Balancing the Groundwater Budget: International Association of Hydrogeologists Groundwater Conference*, Darwin, Australia, pp. 12–17.

Davidson, W. (1995), Hydrogeology and groundwater resources of the Perth Region, Western Australia, *Bull. 142*, Western Australia Geol. Surv., Perth, Australia.

Davis, J., and A. Annan (1989), Ground-penetrating radar for high-resolution mapping of soil and rock stratigraphy, *Geophys. Prospect.*, *37*(5), 531–551.

Day-Lewis, F., J. Lane Jr., J. Harris, and S. Gorelick (2003), Time-lapse imaging of saline-tracer transport in fractured rock using difference-attenuation radar tomography, *Water Resour. Res.*, *39*(10), 1290, doi:10.1029/2002WR001722.

Deiana, R., G. Cassiani, A. Kemna, A. Villa, V. Bruno, and A. Bagliani (2007), An experiment of non invasive characterization of the vadose zone via water injection and cross-hole time-lapse geophysical monitoring, *Near Surf. Geophys.*, *5*(3), 183–194.

Farmani, M., H. Keers, and N. Kitterød (2008), Time-lapse gpr tomography of unsaturated water flow in an ice-contact delta, *Vadose Zone J.*, *7*(1), 272–283.

Farrington, P., E. Greenwood, G. Bartle, J. Beresford, and G. Watson (1989), Evaporation from Banksia woodland on a groundwater mound, *J. Hydrol.*, *105*(1–2), 173–186.

Farrington, P., G. Watson, G. Bartle, and E. Greenwood (1990), Evaporation from dampland vegetation on a groundwater mound, *J. Hydrol.*, *115*(1–4), 65–75.

Froend, R. H., M. Davies, W. Stock, M. Martin, C. Robertson, D. Eamus, and K. Smettem (2010), Environmentally sympathetic groundwater production: Is it possible to maintain abstraction in areas with vulnerable phreatophytic vegetation?, paper presented at Groundwater 2010: The Challenges of Sustainable Management, Canberra, Australia.

Hubbard, S., J. Peterson, E. Majer, P. Zawislanski, K. Williams, J. Roberts, and F. Wobber (1997), Estimation of permeable pathways and water content using tomographic radar data, *Leading Edge*, *16*, 1623.

Huisman, J. A., S. S. Hubbard, J. D. Redman, and A. P. Annan (2003), Measuring soil water content with ground penetrating radar: A review, *Vadose Zone J.*, *2*(4), 476–491, doi:10.2113/2.4.476.

Irving, J. D., M. D. Knoll, and R. J. Knight (2007), Improving crosshole radar velocity tomograms: A new approach to incorporating high-angle traveltime data, *Geophysics*, *72*(4), J31–J41.

Kundzewicz, Z., L. Mata, N. Arnell, P. Dll, P. Kabat, B. Jimnez, K. Miller, T. Oki, Z. Sen, and I. Shiklomanov (2007), Freshwater resources and their management, in *Climate Change 2007: Impacts, Adaptation and Vulnerability. Contribution of Working Group II to the Fourth Assessment Report of the Intergovernmental Panel on Climate Change*, Parry, ML, OF Canziani, JP Palutikof, CE Hanson, and PJ van der Linden, pp. 173–210, Cambridge Univ. Press, Cambridge, U. K.

Lambot, S., A. Binley, E. Slob, and S. Hubbard (2008), Ground penetrating radar in hydrogeophysics, *Vadose Zone J.*, *7*(1), 137–139.

McArthur, W. M., and E. Bettenay (1974), The development and distribution of the soils of the swan coastal plain, Western Australia, *Soil Publ. 16*, Commonwealth Scientific and Industrial Research Organisation (CSIRO), Melbourne, Australia.

McHugh, S. (2011), Perth shallow groundwater systems investigation: Lexia wetlands, *Hydrogeol. Rec. Ser., HG 44*, Dep. of Water, Western Australia, Australia.

McHugh, S., and M. Hammond (2011), Perth shallow groundwater systems investigation: Tangletoe swamp, *Hydrogeol. Rec. Ser., HG 49*, Dep. of Water, Western Australia, Australia.

Olhoeft, G. (1981), Electrical properties of rocks, in *Physical Properties of Rocks and Minerals*, vol. 2, edited by Y. S. Touloukian, W. R. Judd, and R. F. Roy, pp. 257–297, McGraw-Hill, New York.

Peterson, J. (2001), Pre-inversion corrections and analysis of radar tomographic data, *J. Environ. Eng. Geophys.*, *6*, 1.

Pigois, J.-P. (2010), North Gnangara bore completion report, *Hydrogeol. Rec. Ser., HR 277*, Dep. of Water, Western Australia, Australia.

Rucker, D. F., and T. P. A. Ferre (2003), Near-surface water content estimation with borehole ground penetrating radar using critically refracted waves, *Vadose Zone J.*, *2*(2), 247–252, doi:10.2113/2.2.247.

Scanlon, B., R. Healy, and P. Cook (2002), Choosing appropriate techniques for quantifying groundwater recharge, *Hydrogeol. J.*, *10*(1), 18–39.

Searle, J., and G. Bathols (2009), Bore completion report for the shallow groundwater system investigation stage 2, *Hydrogeol. Rec. Ser., HR 276*, Dep. of Water, Perth, Western Australia, Australia.

Sharma, M., M. Bari, and J. Byrne (1991), Dynamics of seasonal recharge beneath a semiarid vegetation on the Gnangara mound, Western Australia, *Hydrol. Processes*, *5*(4), 383–398.

Silberstein, R., A. Barr, G. Hodgson, D. Pollock, R. Salama, and T. Hatton (2009), A vertical flux model for the perth groundwater region, *Hydrogeol. Rec. Ser., HG 33*, Dep. of Water, Western Australia, Australia.

Singh, B., and S. Wong (2010), Acid sulfate soils in the Perth metropolitan area of Western Australia, paper presented at 19th World Congress of Soil Science, Soil Solutions for a Changing World, Brisbane, Australia, 16 Aug.

Steelman, C., and A. Endres (2011), Comparison of petrophysical relationships for soil moisture estimation using gpr ground waves, *Vadose Zone J.*, *10*(1), 270–285.

Strobach, E. (2013), Hydrogeophysical investigation of groundwater recharge into the Gnangara mound, PhD thesis, Dep. of Explor. Geophys., Curtin Univ., West. Aust. Sch. of Mines, Perth, Western Australia.

Strobach, E., B. Harris, J. Dupuis, A. Kepic, and M. Martin (2010a), Gpr for large-scale estimation of groundwater recharge distribution, in *13th International Conference on Ground Penetrating Radar (GPR)*, pp. 1–6, Institute of Electrical and Electronics Engineers, Lecce, Italy.

Strobach, E., B. Harris, J. Dupuis, A. Kepic, and M. Martin (2010b), Ground-penetrating radar for delineation of hydraulically significant layers in the unsaturated zone of the Gnangara mound, WA, in *21st ASEG Conference Extended Abstracts*, pp. 1–4, CSIRO, Melbourne, Australia.

Strobach, E., B. D. Harris, J. C. Dupuis, A. W. Kepic, and M. W. Martin (2011), Estimation of water content in partially saturated soil horizons with ground-penetrating radar, paper presented at 73rd EAGE Conference and Exhibition, Vienna, 23–25 May.

Strobach, E., B. D. Harris, J. Christian Dupuis, A. W. Kepic, and M. W. Martin (2012a), Cross well radar and vertical radar profiling methods for time lapse monitoring of rainfall infiltration, in *22nd ASEG Conference Extended Abstracts*, CSIRO, pp. 1–4.

Strobach, E., B. D. Harris, J. C. Dupuis, A. W. Kepic, and M. W. Martin (2012b), Time-lapse borehole radar measurements in a sandy groundwater system during a winter recharge cycle, in *14th International Conference on Ground Penetrating Radar (GPR)*, pp. 1–6, Institute of Electrical and Electronics Engineers, Shanghai, China.

Strobach, E., B. D. Harris, J. C. Dupuis, and A. W. Kepic (2013), Waveguide properties recovered from shallow diffractions in common offset gpr, *J. Geophys. Res.*, *118*, 39–50, doi:10.1029/2012JB009448.

Thompson, C. (1992), Genesis of podzols on coastal dunes in southern Queensland: I. Field relationships and profile morphology, *Soil Res.*, *30*(5), 593–613.

Timbal, B., J. M. Arblaster, and S. Power (2006), Attribution of the late-twentieth-century rainfall decline in southwest Australia, *J. Clim.*, *19*(10), 2046–2062.

Topp, G. C., J. L. Davis, and A. P. Annan (1980), Electromagnetic determination of soil water content: Measurements in coaxial transmission lines, *Water Resour. Res.*, *16*(3), 574–582.

Tronicke, J., and M. D. Knoll (2005), Vertical radar profiling; influence of survey geometry on first-arrival traveltimes and amplitudes, *J. Appl. Geophys.*, *57*(3), 179–191.

van Dam, R. L., W. Schlager, M. J. Dekkers, and J. A. Huisman (2002), Iron oxides as a cause of gpr reflections, *Geophysics*, *67*(2), 536–545.

Verboom, W., and J. Pate (2006), Bioengineering of soil profiles in semiarid ecosystems: The phytotarium concept. A review, *Plant Soil*, *289*(1), 71–102.

Xu, C., M. Canci, M. Martin, M. Donnelly, and R. Stokes (2008), Perth regional aquifer modelling system (prams) model development: Application of the vertical flux model, *Hydrogeol. Rec. Ser. HG 27*, Dep. of Water, Western Australia, Australia.

Yesertener, C. (2002), Declining water levels in the Gnangara and Jandakot groundwater mounds (stage i), *Hydrol. and Water Resour. Branch, HR 199*, Dep. of Water, Western Australia, Australia.